Partial Differential Equations in Applied Mathematics 11 (2024) 100760

Contents lists available at ScienceDirect

Partial Differential Equations in Applied Mathematics

journal homepage: www.elsevier.com/locate/padiff

Comparative Analysis with Data Prediction of Non-linear Radiative Nano Second-Grade and Newtonian Fluid in Presence of Sinusoidal Magnetic Force

Sarder Firoz Ahmmed [a], Md. Yousuf Ali [b], Sk. Reza-E-Rabbi [a,*]

[a] Mathematics Discipline, Khulna University, Khulna, 9208, Bangladesh

[b] Department of Computer Science and Engineering, Daffodil International University, Dhaka, 1216, Bangladesh

ARTICLE INFO

Keywords:
Newtonian Fluid
Second-Grade Fluid
periodic MHD
Nonlinear Radiation
Heat and Mass Transfer
Data Prediction

ABSTRACT

This study aims to enhance the comprehension of the fundamental fluid behavior by comparing Newtonian fluid with second-grade fluid under the influence of periodic magnetic fields, nonlinear radiative nanomaterial, and a porous stretched surface featuring a heat source. The governing equations' dimensionless forms are generated by applying the proper transformations, and the explicit finite difference (EFD) method is used to solve the numerically-derived solution while carefully maintaining stability and convergence standards. The results include velocity, heat, and mass transfer oscillation profiles; streamlines, and isothermal lines. Nusselt and Sherwood numbers are correlated with different factors according to tabular studies, and data prediction and regression are done using graphical representations. This study revealed that, in contrast to Newtonian fluid, second-grade fluid flow elevates velocity profiles with variations in chemical reaction parameters and mass Grashof numbers. Conversely, the thermal non-linear radiation and heat source in second-grade fluid particles effectively enhance the temperature field, although the temperature increase is more pronounced in Newtonian fluid compared to second-grade fluid. Also, second-grade fluid flow exhibits a lower mass transmission rate but higher stress sharing and heat transmission rates compared to Newtonian fluid flow. The implications of this research may impact prostate cancer treatment, as cancer patients have already benefited from the use of magnetic fields to regulate drug release from nanoparticles. Although the greater stress sharing and heat transmission rates may be used for targeted therapy, the lower mass transmission rate raises the possibility of benefits in controlled release scenarios.

1. Introduction

A particular type of non-Newtonian fluid with unique flow properties is referred to as a "second-grade fluid" in the perspective of rheology. Second-grade fluids have viscosities that vary linearly with the rate of deformation or shear, in disparity to Newtonian fluids, which have a constant viscosity independent of shear rate. This class of fluids is included in the more general category of non-Newtonian fluids, meaning that shear stress is not the only factor influencing their flow characteristics. In the context of their rheological properties, "second-grade" refers to the second order in the expansion of the stress tensor with regard to the rate of strain. Investigation of lower-grade fluids yields useful applications in a variety of scientific and practical domains by providing insights into higher-order fluid dynamics. Analysis of second-grade Nano fluid conducted by Hayat et al.[1] on the incorporation of joule heating using the Buongiorno model revealed that increased estimation of the Reynolds number, magnetic parameter, and radiation parameter increases entropy. The buoyancy force on deformable magnetized second-grade Nano fluid was later found also by the authors[2]. Higher values of the viscoelastic parameter led to an uptick in the temperature distribution, according to the study. Heat transfer, mass, and motile microorganisms were investigated by Shafiq et al.[3] in convective second-grade nanofluid flow. It discovered that while bio-convection limits upward movement of nanoparticles at larger Rayleigh numbers, increased buoyancy impedes fluid flow and impacts concentration. According to Li et al.'s[4] MATLAB analysis of the effects of gyrotactic bio-convection on modified second-grade nanofluids, the thermal performance of the base fluid is improved by the addition of nanoparticles with a low volume fraction and strong thermal properties. When

* Corresponding author.
E-mail address: rabbi06@math.ku.ac.bd (Sk. Reza-E-Rabbi).

https://doi.org/10.1016/j.padiff.2024.100760
Received 14 April 2024; Received in revised form 2 June 2024; Accepted 8 June 2024
Available online 9 June 2024

Nomenclature

Variables

x	Cartesian x coordinate
y	Cartesian y coordinate
X	Non-dimensional x coordinate
Y	Non-dimensional y coordinate
c	Dimensional concentration, [mol m^{-3}]
C	Dimensionless concentration, [-]
C_w	Concentration at the surface, [mol m^{-3}]
C_∞	Concentration out of the surface, [mol m^{-3}]
c_p	Specific heat, [$Jkg^{-1}K^{-1}$]
D_B	Coefficient of Brownian diffusion, [m^2s^{-1}]
g	Gravitational acceleration, [ms^{-2}]
u	Velocity component in x direction, [ms^{-1}]
U	Non-dimensional velocity component, [-]
κ	Boltzmann constant $1.3805 \times 10^{-23} JK^{-1}$
T	Fluid temperature, [K]
T_w	Temperature at the surface, [K]
T_∞	Temperature away from the surface, [K]
Cf	Skin friction coefficient, [-]
q_r	Radiative heat flux, [kgm^{-2}]
D_T	Coefficient of thermophoresis diffusion, [m^2s^{-1}]
t	Dimensional time, [s]
B_0	Magnetic component, [Wbm^{-2}]
Q	Heat source parameter, [-]
k	Thermal conductivity, [$Wm^{-1}K^{-1}$]
v	Velocity component in y direction, [ms^{-1}]
V	Non-dimensional velocity component, [-]

Parameters and Numbers

Pr	Prandtl number, [-]
Gr	Thermal Grashof number, [-]
Rd	Radiation parameter, [-]
Sh	Sherwood number, [-]
Q	Heat source parameter, [-]
Ec	Eckert number, [-]
Gm	Mass Grashof number, [-]
CR	Chemical reaction parameter, [-]
M	Magnetic parameter, [-]
Le	Lewis number, [-]
Rb	Brownian parameter, [-]
Rt	Thermophoresis parameter, [-]
Nu	Nusselt number, [-]
Sg	Second-grade fluid parameter,[-]

Greek Symbols

υ	Kinematic viscosity, [m^2s^{-1}]
λ	Relaxation time effect, [s]
β_C	Mass distribution coefficient
ρ	Fluid density, [kgm^{-3}]
σ	Stefan-Boltzmann constant, [$Wm^{-2}K^{-4}$]
β_T	Heat distribution coefficient
θ_w	Temperature differences
δ	Temperature related parameter
τ	Dimensionless time
α	porosity parameter, [-]
θ	Non-dimensional temperature

Kalaivanan et al.[5] studied second-grade fluid flow with activation energy and nanomaterial control, authors saw that activation energy increased the rate of local heat transfer. Alumina and copper nanoparticle-containing second-grade nanofluids were studied by Jamshed et al.[6] in non-Newtonian engine oil. It found that Cu-EO nanofluids had greater heat transfer rates than Al_2O_3-EO nanofluids. In order to account for heat and mass transfer, Khan et al.'s[7] work on second-grade fluid combines the ideas of Cattaneo-Christov heat flux with generalized Fick's relations and the outcomes implies that the temperature distribution of nanoparticles enhances with an increase in the stretching parameter. The heat transfer properties and flow of a Magneto hydrodynamics (MHD) hybrid second-grade Nano fluid through a convectively heated permeable shrinking/stretching sheet were the subject of Nadeem et al.'s[8] study. The findings indicate that there is a positive correlation between the volume percentage of nanoparticles in the hybrid nano fluid and the rate of heat transmission. Sunthrayuth et al.[9] investigated a second grade MHD Nano fluid and used the RKF 45 method and shot methodology to demonstrate that larger mass transfer happened for fluid flow with consolidation condition at increased levels of strength of heterogeneous as well as homogeneous response parameters. According to Basit et al.'s[10] study on second-grade Nano fluid, Ag-H_2O Nano fluid has a greater temperature than Cu-H_2O and TiO_2-H_2O nanoparticles, although its velocity indicates the reverse.

A Newtonian fluid is a type of fluid that exhibits constant viscosity, regardless of the applied shear stress or strain rate. In simpler terms, when a force is applied to a Newtonian fluid, its response in terms of flow is directly proportional to the force applied. This means that the fluid's viscosity, or resistance to flow, remains constant under different levels of shear force, making its behavior predictable and linear. In contrast to non-Newtonian fluids, which can show variable viscosity under different conditions, Newtonian fluids adhere to a straightforward relationship between stress and strain in terms of fluid flow. The mixing efficiency of blood, a non-Newtonian fluid, was shown to be lower than that of a Newtonian fluid, according to research by Bayareh et al.[11]. A computer study of unsteady natural convective flow in a square enclosure by Pishkar et al.[12] showed that pseudo plastic non-Newtonian fluids display improved heat transfer whereas dilatant non-Newtonian fluids show reduced heat transfer because to oscillating heat flux. The behavior of elastic and viscous fluids in an entrance vortex expansion is studied by Tseng[13], who points out that stable convergence and consistent findings with viscoelastic constitutive equations at large Deborah numbers are difficult to achieve. Jaszczur et al.[14] aimed to study the flow dynamics of Newtonian fluids in a mechanically agitated tank using a new impeller design, finding that the impeller-to-fluid ratio and the distance between the impeller and the vessel bottom significantly influence mixing effectiveness. According to de Goede et al.'s[15] research, blood can be thought of as a Newtonian fluid that spreads on fabrics similarly to smooth surfaces. Moreover, Lattice entropy According to Boltzmann simulations, more viscous losses within the droplet during spreading is the cause of the decreased droplet spreading ratio on fabrics. In addition to focusing on the pressure-driven transport of a multilayer system made up of Newtonian and non-Newtonian fluids in a narrow fluidic configuration, Kumar et al.'s[16] study also demonstrates how rheology can significantly alter flow velocity, which in turn amplifies micro-pumping phenomena. Using numerical simulations, Aerosemena et al.[17] investigated the turbulent channel flow of generalized Newtonian fluids at low Reynolds numbers, discovering mechanisms of drag reduction from shear-thinning behavior that reduce turbulence and near-wall structures. The flow of these fluids through thin elastic tubes was studied by Anand et al.[18], who emphasized the significance of boundary layers for clamping and used ANSYS simulations to validate their hypothesis. Shuguang and Dimitreinko[19] examined the effects of viscosity and permeability on the behavior of these fluids as they modelled their filtering in porous media. Reyes et al.[20] experimented with a parameterized projection-based model reduction

Table 1
The contents of the current project are compared to those of previous scholarly articles.

Authors	NF	SGF	PMHD	NLR	HG	PM	DP
Hayat et al. [2]	×	√	×	×	×	×	×
Shafiq et al. [3]	√	√	×	√	√	×	×
Li et al. [4]	×	√	×	√	×	×	×
Kalaivanan et al. [5]	√	×	×	√	√	×	×
Jamshed et al. [6]	×	√	√	√	×	×	×
Jaszczur et al. [14]	√	×	×	×	×	×	×
Al-Mamun et al. [34]	×	×	√	×	√	×	×
Reza-E-Rabbi et al. [35]	×	×	√	√	×	×	×
Saeed et al. [39]	√	√	×	√	×	√	×
Awan et al. [40]	×	√	×	×	×	×	×
Present Work	√	√	√	√	√	√	√

**Abbreviation: NF-Newtonian Fluid; SGF- Second-Grade Fluid; PMHD- Periodic MHD; NLR-Non-Linear Radiation; HG-Heat Generation; PM-Porous Medium; DP-Data Prediction; √ - Present; × - Absent.

method for solving time-dependent generalized Newtonian fluids.

Nonlinear radiation refers to the study of radiation processes that exhibit nonlinearity in their behavior, deviating from the linear relationships typically observed in conventional radiation phenomena. When Rashid et al.[21] looked into reversible joule heating, nonlinear thermal radiation, and viscous dissipation, researchers observed that entropy growth rates increased with solid nanoparticle volume percentage and Brinkman number, which went against Bejan number expectations. Using gyrotactic microorganisms in an electrically conductive Casson nanofluid, Oyelakin et al.[22] investigated the effects of shifting transport characteristics and nonlinear radiation on the two-dimensional flow of the fluid along a moving wedge. It found that injection flow and concentration differences caused a small drop in microorganism density. Incorporating hybrid nanomaterial's increases axial velocity, according to research by Farooq et al.[23], who used the Built-in-Shooting approach to provide precise numerical solutions for flow issues. In order to account for nonlinear thermal radiation for bio convection processes in engineering and industrial systems, Al-Khaled et al.[24] recommended updating the energy equation. The existence of the radiation parameter, according to the results, enhanced heat transmission. Next, a numerical study of three-dimensional Eyring-Powell over nonlinear radiative Nano fluid with component heat and mass fluxes was carried out by Muhammad et al.[25]. The authors demonstrate that the radiation parameter boosts the fluid's mobility between the particles. Mabood et al.[26] assessed nonlinear thermal radiation and melting heat transfer; the results suggested that an upsurge in nonlinear thermal radiation leads to a thicker boundary layer. The nonlinear radiation parameter improves the temperature profile, as shown by Kataria et al.'s[27] analysis of the energy equation's impacts with convective boundary conditions, thermal nonlinear radiation, and Joule heating. Applying the shooting approach, Shafiq et al.[28] discovered that heat transfer rates in a Casson cobalt ferrite nanofluid across a spinning surface rise with increasing solid volume fractions. As the fraction of nanoparticles in a given volume increases, Khan et al.[29] found that radial velocity declines while temperature and azimuthal velocity rise in non-Newtonian nanofluids. In spite of an increased reaction rate in the presence of a chemical reaction, Gangadhar et al.'s[30] study of the viscoelastic characteristics of an axisymmetric, incompressible Casson-Maxwell nano liquid flow between two stationary discs revealed that raising the radiation parameter and Brownian motion constant improves the temperature distribution of nanoparticles. After investigating MHD non-Newtonian nanofluid flow with Arrhenius activation energy, Ahmed et al.[31] came to the conclusion that activation energy has a major impact on the interaction between Maxwell fluid and nonlinear radiation, which may have implications for the industrial sector and for the treatment of cancer.

Periodic MHD (Magneto hydrodynamic) fluid refers to a specialized class of fluids that combines the principles of magnetism and fluid dynamics within a periodic structure. MHD itself explores the behavior of electrically conducting fluids, such as plasmas, liquid metals, or ionized gases, in the presence of magnetic fields. When this concept is extended to periodic MHD fluid, it implies that the system exhibits periodic or repeating patterns, adding an additional layer of complexity to the study. This field of study is particularly relevant in understanding natural occurrences, such as the magnetic fields within the Earth's core or the dynamics of plasmas in astrophysical objects, where periodicity plays a crucial role. Analyzing the behavior of unstable magneto hydrodynamic free convective flow was the primary goal of Nandi and Kumbhakar's[32] study. Among the main conclusions of Achogo et al.[33] about the periodic behavior of MHD non-Newtonian fluid flow was that an increase in permeability led to an increase in velocity, while an increase in the magnetic field resulted in a drop in velocity. Al-Mamun

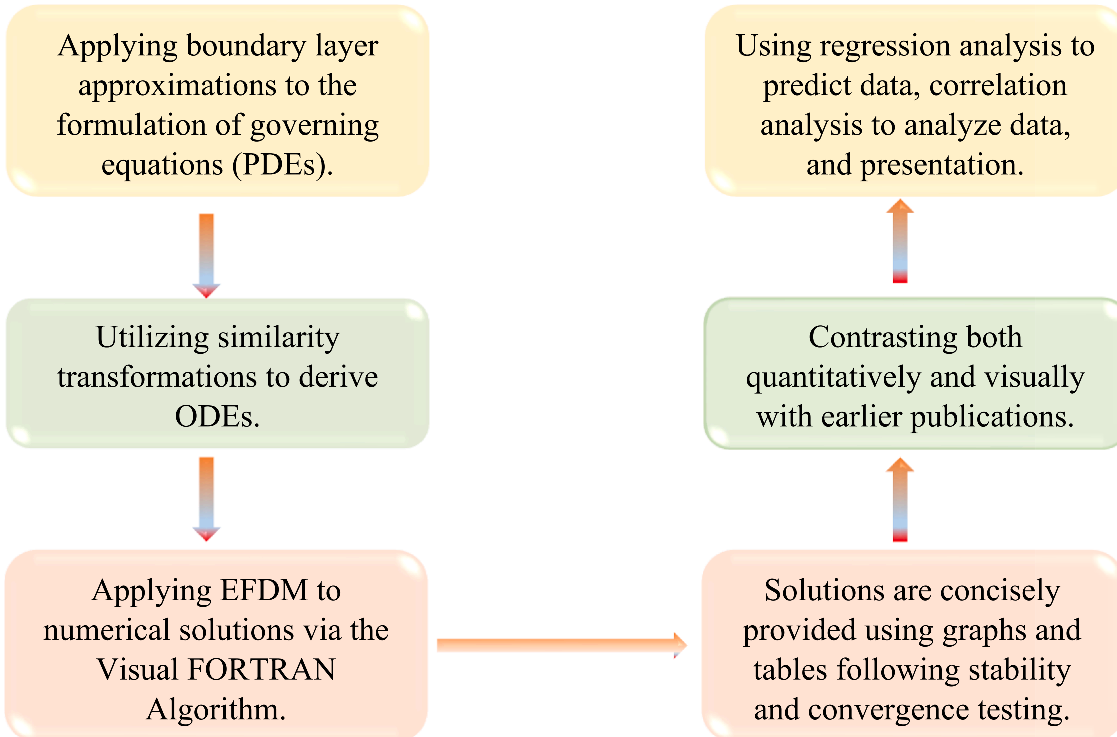

Fig. 1. A flowchart of the methodology.

et al.[34] examined the periodic MHD Casson fluid flow and conjectured that the Lorentz force has a considerable impact on the depiction of the flow field, notably in terms of streamlines and isotherms. Apart from using the EFD approach, research on the characterization of non-Newtonian periodic MHD flow by Reza-E Rabbi et al.[35] shows that thermophoresis processes and Brownian motion of Casson fluid particles boost the temperature field in the presence of nonlinear radiation. After studying the entrained flow and heat transfer in a Newtonian fluid along a thermally and electrically conducting cone in porous media, Ashraf et al.[36] came to the conclusion that the temperature and main stream velocity drop as the surface temperature parameters increase. In their investigation of the effects of triple diffusion and a periodic magnetic field on bio convection flow through an Eyring-Powell fluid surrounding a rotating cone containing oxytactic bacteria, Patil et al.[37] discovered that the density profile and microorganism count are influenced by the Peclet number (Pe) and microbial density differences. The effects of Joule heating and periodic MHD on heat transfer and current density in a magnetized cylinder were examined by Khedher et al.[38], who found that Joule heating greatly improves the temperature distribution. Increases in heat transfer in MHD flow are exhibited by thermoelectric and radiation effects, as reported by Yousuf Ali et al.[39], who noted a decrease in the flow of Nano fluid when thermal radiation increases. Another research[40] looked at the combined effects of thermoelectric and thermal radiation processes on the hydro-magnetic flow of Casson fluid over a stretched sheet. It showed that the non-Newtonian (Casson) fluid was more affected than the Newtonian fluid. Researchers[41] looked at how radiation and Hall current affected Bingham fluid, highlighting how important the stretching rate is in Bingham fluid compared to Newtonian fluid. By using sinusoidal boundary conditions to study heat and mass transport in Casson hydro-magnetic fluid flow, Islam et al.[42] found that adding the porosity parameter reduced skin friction and increasing the Sherwood number increased the Lewis number and chemical reaction parameter. Another work[43] that employed numerical modelling to simulate the flow of a non-Newtonian fluid in the presence of nonlinear thermal radiation showed an increase in the Lorentz force operating on the velocity distribution due to nonlinear radiation. The effects of thermophoresis, multi-buoyancy forces, Brownian motion, and magneto hydrodynamic Prandtl hybrid nanofluid over a stretched surface with chemical reactions and bio convection are examined by the authors[44–48] in relation to MHD Prandtl fluid and heat transfer in 3D rotating Williamson hybrid nanofluid with Darcy-Forchheimer. Additionally, nonlinear thermal radiation, chemical reactions on a stretched sheet, bio-convection in Williamson nanofluid flow, and changing copper nanoparticle radii in non-Newtonian nanofluid flow are explored. Important discoveries show that while more thermal and concentration stratification lowers temperature and concentration, higher thermal radiation parameters raise temperature profiles. Higher Prandtl parameter values result in enhanced velocity profiles, whereas higher Williamson fluid and magnetic parameter values result in decreased velocity profiles. Higher Forchheimer number (Fr) and material parameter (Δ) also lower temperatures. The study conducted by the researchers[49–53] looks into the following topics: bio convection of non-homogeneous hybrid nanofluids that are not steady; the effect of concentrations of hybrid nanoparticles and power-law index on non-Newtonian hybrid nanofluid behavior; gyrotactic microorganisms on bio convection in electromagnet hydrodynamic hybrid nanofluid; and ternary hybrid nanofluid flow with micro channel-based microorganisms. The temperature distribution decreases with increasing Prandtl number, ternary hybrid nanofluids exhibit higher temperatures than regular nanofluids, and higher concentration ratio parameters maximize entropy generation. Mass transfer rates also decrease by 25.76% with chemical reactions in the presence of activation energy and by 62.22% without it. As (D_B) values rise, there is an increase in nanoparticle number but a decrease in heat flow, bacterial density, and temperature.

This research examines how heat production, nonlinear radiation, and periodic MHD effects affect second-grade nanofluid flow while comparing second-grade fluid dynamics to Newtonian flow. Research gaps found in previous studies are shown in Table 1. These gaps inspired this study, which expands on Reza-E-Rabbi et al.'s[35] work by examining the effects of time-dependent, nonlinear radiative second-grade nanofluid flow across a porous stretched surface. This investigation yields several important observations. Unlike Newtonian fluid flow,

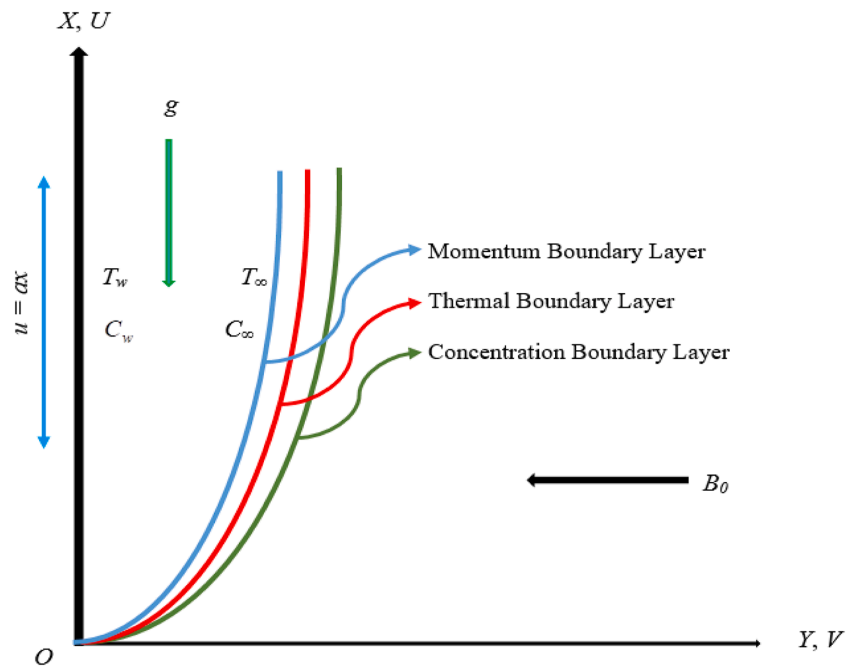

Fig. 2. Diagrammatic representation.

second-grade fluid flow notably improves velocity profiles with different mass Grashof numbers and chemical reaction parameters. In addition, compared to Newtonian fluids, second-grade fluids have a lower Sherwood number but quicker rates of heat transport and stress distribution. These results are critical to the design of precisely controlled temperature systems, especially in the biomedical domain where polymer synthesis and hyperthermia therapy are involved.

2. Applications

Innovations in basic research and advanced technology are spurred by the pioneering work in second-grade fluid systems. The use of heat sources, non-linear radiation, and sinusoidal magnetic fields to second-grade fluid flow demonstrates adaptability and significant effects, offering novel approaches to a variety of scientific and industrial procedures. This discovery paves the way for revolutionary improvements, from raising heat transfer efficiency in heat exchangers by manipulating magnetic fields to highlighting the critical importance of non-linear radiation in environmental modelling. The applications in the field of biomedicine include treatments for hyperthermia and thermal therapy. Treatment optimization requires a thorough grasp of how radiation interacts with biological tissues in second-grade fluid systems. Investigating second-grade fluid flow in a stretched media is essential for understanding cardiovascular dynamics, especially when considering blood flow and biological fluids. This in turn provides information for medical device optimization. Second-grade fluid systems are a dynamic field that not only influences the direction of scientific research but also offers the possibility of breakthroughs with real-world applications.

3. Methodology

This suggested study builds on previous research endeavors by examining how heat production and sinusoidal magnetic factors affect the time-evolving nonlinear radiative flow of a second-grade Nano fluid along a stretched perimeter. Although the research of Reza-E-Rabbi et al.[35], which primarily focused on the use of Casson Nano fluid as the basic fluid, served as inspiration for this work, it stands out because it focuses on the second-grade Nano fluid. Aspects of heat production and the effects of nonlinear radiation are explored, which were not included in their work. This project uses a numerical simulation-based technique, which means that a thorough numerical strategy is needed to carry it out. For this reason, the explicit finite difference (EFD) method is used. A prominent advantage of using the explicit finite technique is a large decrease in computational time. This approach is affordable and efficient in terms of computation, and it is reasonably easy to set up and programed. To further ensure the correctness of the approach, a stability test is conducted once it has been implemented. Fig. 1 shows how the continuing work has been methodically arranged.

4. Mathematical Analysis

Deliberate attention has been directed towards scrutinizing the dynamics of a two-dimensional, temporally evolving, viscous, and incompressible boundary layer flow featuring chemical reactivity, influenced by nonlinear radiation, and a porous medium. In this particular scenario, a periodic second-grade magneto hydrodynamic (MHD) Nano fluid flow as well as Newtonian fluid flow are applied to a linearly stretched sheet located at the plane $y = 0$, endowed with the ability to either generate or absorb internal heat. Fig. 2 delineates the intricate physical flow configuration under diverse pivotal circumstances. To attain a more profound comprehension of the subject, a Cartesian coordinate system has been deployed, with the x-coordinate extending along the axial flow direction and the y-coordinate running perpendicular to the sheet. Additionally, the flow is induced by the stretched sheet in the x-direction. In this context, the concentration, temperature, and ambient velocity of the fluid are assumed to be represented by $u = ax$, T_∞, and C_∞, respectively.

The resulting equations determine the behavior of the second-grade Nano fluid across the stretching sheet assuming these assumptions and appropriate boundary layer approximations[7,8,35,42]:

$$\frac{\partial u}{\partial x} + \frac{\partial v}{\partial y} = 0 \tag{1}$$

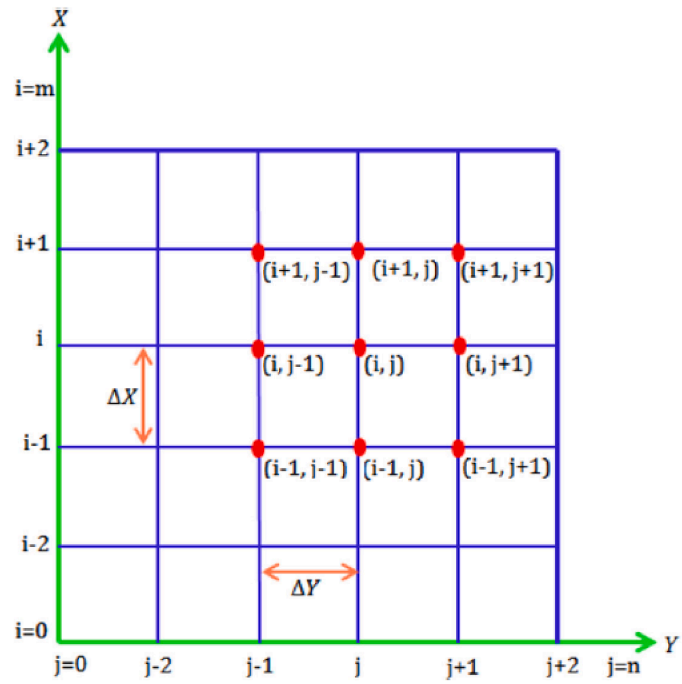

Fig. 3. Grid spacing with finite differences[35].

$$\frac{\partial u}{\partial t}+u\frac{\partial u}{\partial x}+v\frac{\partial u}{\partial y}=\left[\begin{array}{l} \upsilon\frac{\partial^2 u}{\partial y^2}+\frac{\alpha_1}{\rho}\left(u\frac{\partial^3 u}{\partial x\partial y^2}+\frac{\partial u}{\partial x}\frac{\partial^2 u}{\partial y^2}-\frac{\partial u}{\partial y}\frac{\partial^2 u}{\partial x\partial y}+v\frac{\partial^3 u}{\partial y^3}\right) \\ +g\beta_T(T-T_\infty)+g\beta_C(C-C_\infty)-\frac{\sigma B_0^2}{\rho}\sin^2\left(\frac{\pi x}{\lambda}\right)u-\frac{\upsilon}{k_1}u \end{array}\right] \tag{2}$$

$$\frac{\partial T}{\partial t}+u\frac{\partial T}{\partial x}+v\frac{\partial T}{\partial y}=\left[\begin{array}{l} \frac{\kappa}{\rho c_p}\frac{\partial^2 T}{\partial y^2}+\frac{\alpha_1}{\rho c_p}\frac{\partial u}{\partial y}\left\{\frac{\partial}{\partial y}\left(u\frac{\partial u}{\partial x}+v\frac{\partial u}{\partial y}\right)\right\}+\frac{Q'}{\rho c_p}(T-T_\infty) \\ +\frac{\upsilon}{c_p}\left(\frac{\partial u}{\partial y}\right)^2+\frac{\varepsilon D_T}{T_\infty}\left(\frac{\partial T}{\partial y}\right)^2-\frac{1}{\rho c_p}\frac{\partial q_r}{\partial y}+\varepsilon D_B\left(\frac{\partial T}{\partial y}\frac{\partial C}{\partial y}\right) \end{array}\right] \tag{3}$$

$$\frac{\partial C}{\partial t}+u\frac{\partial C}{\partial x}+v\frac{\partial C}{\partial y}=\frac{D_T}{T_\infty}\frac{\partial^2 T}{\partial y^2}-\sigma^2(C-C_\infty)+D_B\frac{\partial^2 C}{\partial y^2} \tag{4}$$

Initial boundary conditions:

$$\left.\begin{array}{l} t=0, u=ax, T=T_\infty, v=0, C=C_\infty \text{everywhere} \\ t\geq 0, u=0, T=T_\infty, v=0, C=C_\infty \text{at} x=0 \\ u=ax, T=T_w, v=0, C=C_w \text{at} y=0 \\ u=0, T\to T, v=0_\infty, C\to C_\infty \text{as} y\to\infty \end{array}\right\} \tag{5}$$

The velocity factors along the x and y axes are represented, respectively, by the symbols u and v; $a>0$ denotes the stretching constant, $a<0$ denotes the shrinking factor, and κ stands for heat conductivity. D_B and D_T stand for the thermophoresis and Brownian diffusion coefficients, respectively.

A typical instance of the Roseland approximation for radiative heat flow looks like this:

$$q_r=-\frac{4\sigma'}{3k^*}\frac{\partial T^4}{\partial y}=-\frac{4\sigma'}{3k^*}\left(4T^3\frac{\partial T}{\partial y}\right)$$

Thus, the following can be used to describe the nonlinear radiation term:

$$\frac{\partial q_r}{\partial y}=-\frac{16\sigma'}{3k^*}\frac{\partial}{\partial y}\left(T^3\frac{\partial T}{\partial y}\right)=-\frac{16\sigma'}{3k^*}\left[T^3\frac{\partial^2 T}{\partial y^2}+3T^2\left(\frac{\partial T}{\partial y}\right)^2\right]$$

The equation (3) thus takes on the following form:

$$\frac{\partial T}{\partial t}+u\frac{\partial T}{\partial x}+v\frac{\partial T}{\partial y}=\left[\begin{array}{c} \frac{\kappa}{\rho c_p}\frac{\partial^2 T}{\partial y^2}+\frac{\alpha_1}{\rho c_p}\frac{\partial u}{\partial y}\left\{\frac{\partial}{\partial y}\left(u\frac{\partial u}{\partial x}+v\frac{\partial u}{\partial y}\right)\right\}-\frac{\upsilon}{c_p}\left(\frac{\partial u}{\partial y}\right)^2 \\ +\frac{\varepsilon D_T}{T_\infty}\left(\frac{\partial T}{\partial y}\right)^2+\varepsilon D_B\left(\frac{\partial C}{\partial y}\frac{\partial T}{\partial y}\right) \\ +\frac{16\sigma'}{3\rho c_p k^*}\left\{T^3\frac{\partial^2 T}{\partial y^2}+3T^2\left(\frac{\partial T}{\partial y}\right)^2\right\} \end{array}\right] \tag{6}$$

Regarding this fluid model, the non-dimensional parameters are as follows:

$$\begin{array}{l} u=\frac{\upsilon}{\lambda}Gr^{1/2}U, v=\frac{\upsilon}{\lambda}Gr^{1/4}V, Y=\frac{y}{\lambda}Gr^{1/4}, X=\frac{x}{\lambda}, \tau=\frac{\upsilon}{\lambda^2}Gr^{1/2}t \\ \theta=\frac{T-T_\infty}{T_w-T_\infty}, \phi=\frac{C-C_\infty}{C_w-C_\infty}, \theta_w=\frac{T_w}{T_\infty}, T=[1+(\theta_w-1)\theta]T_\infty \end{array} \tag{7}$$

Therefore, the dimensionless representations of the crucial equations are,

$$\frac{\partial U}{\partial X}+\frac{\partial V}{\partial Y}=0 \tag{8}$$

$$\frac{\partial U}{\partial \tau}+U\frac{\partial U}{\partial X}+V\frac{\partial U}{\partial Y}=\left[\begin{array}{l} Sg\left(U\frac{\partial^3 U}{\partial X\partial Y^2}+\frac{\partial U}{\partial X}\frac{\partial^2 U}{\partial Y^2}-\frac{\partial U}{\partial Y}\frac{\partial^2 U}{\partial X\partial Y}+V\frac{\partial^3 U}{\partial Y^3}\right)\\ +\frac{\partial^2 U}{\partial Y^2}+\theta+\frac{Gm}{Gr}\phi-M^2\sin^2(\pi X)U-\alpha U\end{array}\right] \tag{9}$$

$$\frac{\partial \theta}{\partial \tau}+U\frac{\partial \theta}{\partial X}+V\frac{\partial \theta}{\partial Y}=\left[\begin{array}{l} \frac{1}{\Pr}\left\{1+Rd\{1+(\theta_w-1)\theta\}^3\right\}\frac{\partial^2\theta}{\partial Y^2}\\ +SgEc\frac{\partial U}{\partial Y}\left\{\frac{\partial}{\partial Y}\left(U\frac{\partial U}{\partial X}+V\frac{\partial U}{\partial Y}\right)\right\}\\ +Nb\left(\frac{\partial \phi}{\partial Y}\frac{\partial \theta}{\partial Y}\right)+\left\{Nt+3\frac{Rd}{\Pr}\{1+(\theta_w-1)\theta\}^2\right\}\left(\frac{\partial \theta}{\partial Y}\right)^2\\ +Q\theta+Ec\left(\frac{\partial U}{\partial Y}\right)^2\end{array}\right] \tag{10}$$

$$\frac{\partial \phi}{\partial \tau}+U\frac{\partial \phi}{\partial X}+V\frac{\partial \phi}{\partial Y}=\frac{1}{\mathrm{Pr}Le}\left[\frac{Nt}{Nb}\frac{\partial^2\theta}{\partial Y^2}+\frac{\partial^2\phi}{\partial Y^2}\right]-CR\phi \tag{11}$$

Additionally, the related boundary conditions becomes

$$\left.\begin{array}{l}\tau=0, U=0,\phi=0, V=0,\theta=0\text{everywhere}\\ \tau\ge 0, U=0,\phi=0,V=0,\theta=0\text{at}X=0\\ U=aX=A,\phi=1,V=0,\theta=1\text{at}Y=0\\ U=0,\phi\to 0, V=0,\theta\to 0\text{as}Y\to\infty\end{array}\right\} \tag{12}$$

Where,

$$M^2=\frac{\sigma B_0^2\lambda^2}{\rho\upsilon Gr^{1/2}}, Sg=\frac{A\alpha_1}{\rho\upsilon}, Ec=\frac{\upsilon^2 Gr}{\lambda^2 c_p(T_w-T_\infty)}, Gr=\frac{g\beta_T(T_w-T_\infty)\lambda^3}{\upsilon^2}, Pr=\frac{\rho c_p\upsilon}{\kappa}=\frac{\upsilon}{\alpha},$$

$$Le=\frac{\alpha}{D_B}, Rd=\frac{16\sigma' T_\infty^3}{3k^*\kappa}, Gm=\frac{g\beta_c(C_w-C_\infty)\lambda^3}{\upsilon^2}, Nb=\frac{\varepsilon D_B(C_w-C_\infty)}{\upsilon}, Nt=\frac{\varepsilon D_T(T_w-T_\infty)}{T_\infty\upsilon}, \alpha=\frac{\lambda^2}{k_1 Gr^{1/2}},$$

and $CR=\frac{\sigma^2\lambda^2}{\upsilon Gr^{1/2}}$ are the magnetic parameter, second-grade fluid parameter, Eckert number, thermal Grashof number, Prandtl number, Lewis number, radiation parameter, mass Grashof number, Brownian motion parameter, thermophoresis parameter, porous term and chemical reaction rate parameter respectively.

Furthermore, elucidating the Sherwood number, Nusselt number, and local friction factor entails:

$$Sh=\frac{Gr^{-3/4}}{2\sqrt{2}}\left(\frac{\partial\phi}{\partial Y}\right)_{Y=0}, Nu=\frac{Gr^{-3/4}}{2\sqrt{2}}\left(\frac{\partial\theta}{\partial Y}\right)_{Y=0} \text{ and } Cf=-\frac{Gr^{-3/4}}{2\sqrt{2}}\left(\frac{\partial U}{\partial Y}\right)_{Y=0}$$

5. Numerical Analysis

The method used to solve the dimensionless governing equations (8-11) is explained in this section, along with the related boundary conditions. The time-dependent partial differential equations (PDEs) with boundary conditions are difficult to solve analytically because to the large nonlinearity included in these governing equations. As a result, the running model has been resolved by applying the well-recognized explicit finite difference (EFD) method, a numerical solver. Lines parallel to the X and Y axes discretize the domain inside the boundary layer into squares; the X axis is parallel to the stretching surface, while the Y axis is perpendicular to it (see Fig. 3). Inside this study, the plate dimensions are represented by the numerical values X (corresponding to 10) and Y (corresponding to 25). The intervals inside the grid space are denoted by the values m (set to 125) and n (set to 125).

The formulation of equations (8) through (11) may be achieved by applying the EFD approximation technique.

$$\frac{U_{i,j}-U_{i-1,j}}{\Delta X}+\frac{V_{i,j}-V_{i,j-1}}{\Delta Y}=0 \tag{13}$$

$$\begin{aligned}&U'_{i,j}=U_{i,j}+\theta_{i,j}\Delta\tau+\frac{Gm}{Gr}\phi_{i,j}\Delta\tau-M^2U_{i,j}\sin^2(\pi X)\Delta\tau+\frac{U_{i,j+1}+U_{i,j-1}-2U_{i,j}}{(\Delta Y)^2}\Delta\tau\\ &-\alpha U_{i,j}\Delta\tau-\left(\frac{U_{i,j}-U_{i-1,j}}{\Delta X}\right)U_{i,j}\Delta\tau-\left(\frac{U_{i,j+1}-U_{i,j}}{\Delta Y}\right)V_{i,j}\Delta\tau\\ &+Sg\left\{\begin{array}{c}U_{i,j}\frac{U_{i,j+1}-U_{i-1,j+1}-2U_{i,j}+2U_{i-1,j}+U_{i,j-1}-U_{i-1,j-1}}{\Delta X(\Delta Y)^2}+\\ V_{i,j}\frac{U_{i,j+2}-3U_{i,j+1}+3U_{i,j}-U_{i,j-1}}{(\Delta Y)^3}\\ +\frac{U_{i,j}-U_{i-1,j}}{\Delta X}\frac{U_{i,j+1}+U_{i,j-1}-2U_{i,j}}{(\Delta Y)^2}\\ -\frac{U_{i,j+1}-U_{i,j}}{\Delta Y}\frac{U_{i+1,j+1}-U_{i+1,j-1}-U_{i-1,j+1}+U_{i-1,j-1}}{4\Delta X\Delta Y}\end{array}\right\}\Delta\tau\end{aligned} \tag{14}$$

$$\begin{aligned}\theta'_{i,j}=\theta_{i,j}&+\Delta\tau\left[\frac{\left[1+Rd\{1+(\theta_w-1)\theta_{i,j}\}^3\right]}{\Pr}\left(\frac{\theta_{i,j+1}-2\theta_{i,j}+\theta_{i,j-1}}{(\Delta Y)^2}\right)+Q\theta_{i,j}\right]\\ &+\Delta\tau\left[Ec\left(\frac{U_{i,j+1}-U_{i,j}}{\Delta Y}\right)^2+Nb\left(\frac{\phi_{i,j+1}-\phi_{i,j}}{\Delta Y}\frac{\theta_{i,j+1}-\theta_{i,j}}{\Delta Y}\right)+Nt\left(\frac{\theta_{i,j+1}-\theta_{i,j}}{\Delta Y}\right)^2\right]\\ &+\Delta\tau\left[\frac{Rd\{1+(\theta_w-1)\theta_{i,j}\}^2}{\Pr}\left(\frac{\theta_{i,j+1}-\theta_{i,j}}{\Delta Y}\right)^2-V_{i,j}\left(\frac{\theta_{i,j+1}-\theta_{i,j}}{\Delta Y}\right)-U_{i,j}\left(\frac{\theta_{i,j}-\theta_{i-1,j}}{\Delta X}\right)\right]\\ &+SgEc\Delta\tau\left[\begin{array}{l}\left(\frac{U_{i,j}-U_{i-1,j}}{\Delta X}\right)\left(\frac{U_{i,j+1}-U_{i,j}}{\Delta Y}\right)^2+\left(\frac{V_{i,j+1}-V_{i,j}}{\Delta Y}\right)\left(\frac{U_{i,j+1}-U_{i,j}}{\Delta Y}\right)^2\\ +U_{i,j}\left(\frac{U_{i,j+1}-U_{i,j}}{\Delta Y}\right)\left(\frac{U_{i+1,j+1}-U_{i+1,j-1}-U_{i-1,j+1}+U_{i-1,j-1}}{4\Delta X\Delta Y}\right)\\ +V_{i,j}\left(\frac{U_{i,j+1}+U_{i,j-1}-2U_{i,j}}{(\Delta Y)^2}\right)\left(\frac{U_{i,j+1}-U_{i,j}}{\Delta Y}\right)\end{array}\right]\end{aligned} \tag{15}$$

$$\begin{aligned}\phi'_{i,j}=\phi_{i,j}&+\frac{1}{PrLe}\left[\frac{Nt}{Nb}\left(\frac{\theta_{i,j+1}-2\theta_{i,j}+\theta_{i,j-1}}{(\Delta Y)^2}\right)+\left(\frac{\phi_{i,j+1}-2\phi_{i,j}+\phi_{i,j-1}}{(\Delta Y)^2}\right)\right]\Delta\tau\\ &-CR\phi_{i,j}\Delta\tau-U_{i,j}\left(\frac{\phi_{i,j}-\phi_{i-1,j}}{\Delta X}\right)\Delta\tau-V_{i,j}\left(\frac{\phi_{i,j+1}-\phi_{i,j}}{\Delta Y}\right)\Delta\tau\end{aligned} \tag{16}$$

Also, the boundary conditions,

$$U_{i,0}^n=1,\phi_{i,0}^n=1,\theta_{i,0}^n=1$$
$$U_{i,0}^n=0,\phi_{i,L}^n=0,\theta_{i,L}^n=0\text{where}, L\to\infty$$

Here, i and j are the mesh points along the X and Y axes, respectively.

The time value is represented byτ, which may also be written as$\tau=n\Delta\tau, n\in\mathbb{N}$.

6. Examination of Stability and Convergence

A thorough evaluation of the model's stability and convergence is essential, as it is finished using the Explicit Finite Difference Method (EFDM). By keeping to a certain mesh size, it might be able to meet the stability requirements for the remaining tasks. The stability and convergence assessment do not allow for the use of equation (13). The convergence test and stability analysis commences by employing the dimensionless U, θ, and ϕ procedure, initiating with an assumption involving the known term $e^{i(\alpha X+\beta Y)}$ at time $\tau = 0$ in the Fourier expansion, represented by the variable$i = \sqrt{-1}$. The Fourier expansion for U, θ, and ϕ at any given time τ can now be articulated using Equation (17), while after a time step $\Delta\tau$the Fourier extension for U', θ', and ϕ' is represented by Equation (18).

$$\left.\begin{array}{l} U : D(\tau)e^{i(\alpha X+\beta Y)} \\ \theta : E(\tau)e^{i(\alpha X+\beta Y)} \\ \phi : F(\tau)e^{i(\alpha X+\beta Y)} \end{array}\right\} \tag{17}$$

Again,

$$\left.\begin{array}{l} U' : D'(\tau)e^{i(\alpha X+\beta Y)} \\ \theta' : E'(\tau)e^{i(\alpha X+\beta Y)} \\ \phi' : F'(\tau)e^{i(\alpha X+\beta Y)} \end{array}\right\} \tag{18}$$

Now by substituting the equations (17) and (18) in equations (14) to (16), following equations (19) to (21) are obtained

$$\begin{aligned} D' =& D\left\{1+\left[\frac{2(\cos\beta\Delta Y-1)}{(\Delta Y)^2}-\alpha-M^2\sin^2(\pi X) -V\frac{(e^{i\beta\Delta Y}-1)}{\Delta Y}-U\frac{(1-e^{-i\alpha\Delta X})}{\Delta X}\right]\Delta\tau\right\} \\ &+SgD\left\{\begin{array}{l} U\dfrac{2(1-e^{-i\alpha\Delta X})(\cos\beta\Delta Y-2)}{\Delta X(\Delta Y)^2}+U\dfrac{(1-e^{-i\alpha\Delta X})}{\Delta X}\dfrac{2(\cos\beta\Delta Y-1)}{(\Delta Y)^2} \\ +V\dfrac{2(e^{i\beta\Delta Y}-1)(\cos\beta\Delta Y-2)}{(\Delta Y)^3}-U\dfrac{\sin\alpha\Delta X\sin\beta\Delta Y}{\Delta Y\Delta X}\dfrac{(e^{i\beta\Delta Y}-1)}{\Delta Y} \end{array}\right\}\Delta\tau \\ &+E\Delta\tau+\frac{Gm}{Gr}F\Delta\tau \end{aligned} \tag{19}$$

$$\begin{aligned} E' =& QF\Delta\tau+E\frac{(e^{i\beta\Delta Y}-1)^2}{(\Delta Y)^2}\left[Nt\theta+Nb\phi+\frac{Rd\{1+(\theta_w-1)\theta\}^2}{\Pr}\theta\right]\Delta\tau \\ &+E\left[1+\left\{\frac{1+Rd\{1+(\theta_w-1)\theta\}^3}{\Pr}\frac{2(\cos\beta\Delta Y-1)}{(\Delta Y)^2} -V\frac{(e^{i\beta\Delta Y}-1)}{\Delta Y}-U\frac{(1-e^{-i\alpha\Delta X})}{\Delta X}\right\}\Delta\tau\right] \\ &+DEcU\frac{(e^{i\beta\Delta Y}-1)}{(\Delta Y)^2}\Delta\tau\left\{\left(e^{i\beta\Delta Y}-1\right) +Sg\left[\begin{array}{l}\dfrac{V}{\Delta Y}\left\{\left(e^{i\beta\Delta Y}-1\right)^2+2(\cos\beta\Delta Y-1)\right\} \\ +\dfrac{U}{\Delta X}\left\{\sin\alpha\Delta X\sin\beta\Delta Y+\left(1-e^{-i\alpha\Delta X}\right)\left(e^{i\beta\Delta Y}-1\right)\right\}\end{array}\right]\right\} \end{aligned} \tag{20}$$

$$\begin{aligned} F' =& F\left[1+\left\{\frac{1}{\Pr Le}\frac{2(\cos\beta\Delta Y-1)}{(\Delta Y)^2}-V\frac{(e^{i\beta\Delta Y}-1)}{\Delta Y} -U\frac{(1-e^{-i\alpha\Delta X})}{\Delta X}-CR\right\}\Delta\tau\right] \\ &+E\left[\frac{Nt}{\Pr NbLe}\frac{2(\cos\beta\Delta Y-1)}{(\Delta Y)^2}\right]\Delta\tau \end{aligned} \tag{21}$$

Equations (19)-(21) may also be formulated in the following manner:

$$\left.\begin{array}{l} D' = \Upsilon_1 D+\Upsilon_2 E+\Upsilon_3 F \\ E' = \Upsilon_4 D+\Upsilon_5 E+\Upsilon_6 F \\ F' = \Upsilon_7 E+\Upsilon_8 F \end{array}\right\} \tag{22}$$

Where,

$$\begin{aligned} \Upsilon_1 =& \left\{1+\left[\frac{2(\cos\beta\Delta Y-1)}{(\Delta Y)^2}-\alpha-M^2\sin^2(\pi X) -V\frac{(e^{i\beta\Delta Y}-1)}{\Delta Y}-U\frac{(1-e^{-i\alpha\Delta X})}{\Delta X}\right]\Delta\tau\right\} \\ &+Sg\left\{\begin{array}{l} U\dfrac{2(1-e^{-i\alpha\Delta X})(\cos\beta\Delta Y-2)}{\Delta X(\Delta Y)^2}+U\dfrac{(1-e^{-i\alpha\Delta X})}{\Delta X}\dfrac{2(\cos\beta\Delta Y-1)}{(\Delta Y)^2} \\ +V\dfrac{2(e^{i\beta\Delta Y}-1)(\cos\beta\Delta Y-2)}{(\Delta Y)^3}-U\dfrac{\sin\alpha\Delta X\sin\beta\Delta Y}{\Delta Y\Delta X}\dfrac{(e^{i\beta\Delta Y}-1)}{\Delta Y} \end{array}\right\}\Delta\tau \end{aligned}$$

$$\Upsilon_2 = \Delta\tau; \Upsilon_3 = \frac{Gm}{Gr}\Delta\tau$$

$$\Upsilon_4 = UEc\frac{(e^{i\beta\Delta Y}-1)}{(\Delta Y)^2}\Delta\tau\left\{\left(e^{i\beta\Delta Y}-1\right) +Sg\left[\begin{array}{l}\dfrac{V}{\Delta Y}\left\{\left(e^{i\beta\Delta Y}-1\right)^2+2(\cos\beta\Delta Y-1)\right\} \\ +\dfrac{U}{\Delta X}\left\{\sin\alpha\Delta X\sin\beta\Delta Y+\left(1-e^{-i\alpha\Delta X}\right)\left(e^{i\beta\Delta Y}-1\right)\right\}\end{array}\right]\right\}$$

$$\begin{aligned} \Upsilon_5 =& 1+\frac{(e^{i\beta\Delta Y}-1)^2}{(\Delta Y)^2}\left[Nt\theta+Nb\phi+\frac{Rd\{1+(\theta_w-1)\theta\}^2}{\Pr}\theta\right]\Delta\tau \\ &+\left\{\frac{1+Rd\{1+(\theta_w-1)\theta\}^3}{\Pr}\frac{2(\cos\beta\Delta Y-1)}{(\Delta Y)^2} -V\frac{(e^{i\beta\Delta Y}-1)}{\Delta Y}-U\frac{(1-e^{-i\alpha\Delta X})}{\Delta X}\right\}\Delta\tau \end{aligned}$$

$$\Upsilon_6 = Q\Delta\tau, \Upsilon_7 = \frac{Nt}{\Pr NbLe}\frac{2(\cos\beta\Delta Y-1)}{(\Delta Y)^2}\Delta\tau$$

$$\Upsilon_8 = 1+\left\{\frac{1}{\Pr Le}\frac{2(\cos\beta\Delta Y-1)}{(\Delta Y)^2}-V\frac{(e^{i\beta\Delta Y}-1)}{\Delta Y}-U\frac{(1-e^{-i\alpha\Delta X})}{\Delta X}-CR\right\}\Delta\tau$$

Utilizing the expression provided by equation (23), the representation of equations (22) can be succinctly articulated in matrix notation,

$$\begin{bmatrix} D' \\ E' \\ F' \end{bmatrix} = \begin{bmatrix} \Upsilon_1 & \Upsilon_2 & \Upsilon_3 \\ \Upsilon_4 & \Upsilon_5 & \Upsilon_6 \\ 0 & \Upsilon_7 & \Upsilon_8 \end{bmatrix}\begin{bmatrix} D \\ E \\ F \end{bmatrix} \therefore \eta' = A_M\eta \tag{23}$$

Where,

$$\eta' = \begin{bmatrix} D' \\ E' \\ F' \end{bmatrix}, \Upsilon_M = \begin{bmatrix} \Upsilon_1 & \Upsilon_2 & \Upsilon_3 \\ \Upsilon_4 & \Upsilon_5 & \Upsilon_6 \\ 0 & \Upsilon_7 & \Upsilon_8 \end{bmatrix} \text{ and} \eta = \begin{bmatrix} D \\ E \\ F \end{bmatrix} \tag{24}$$

The complexity introduced by the diverse nature of Υ_M renders the investigation notably challenging. Consequently, to address this challenge, a condensed temporal increment, denoted as$\Delta\tau\rightarrow 0$, has been implemented. This choice leads to the derivation of $\Upsilon_2\rightarrow 0$, $\Upsilon_3\rightarrow 0$, $\Upsilon_4\rightarrow 0$, $\Upsilon_6\rightarrow 0$ and $\Upsilon_7\rightarrow 0$ within the given context.

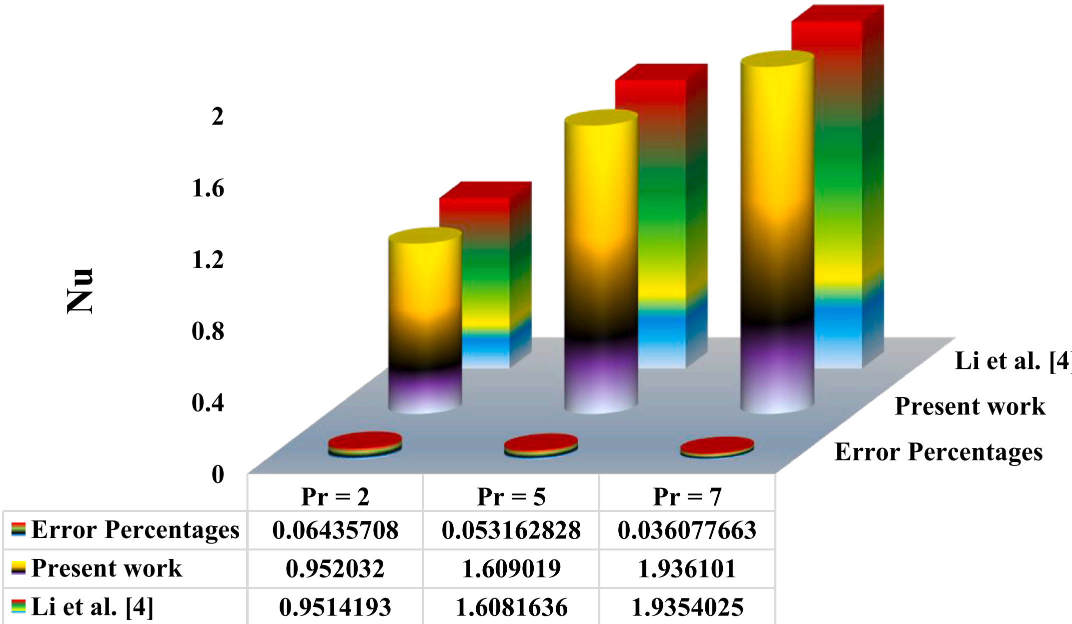

	Pr = 2	Pr = 5	Pr = 7
Error Percentages	0.06435708	0.053162828	0.036077663
Present work	0.952032	1.609019	1.936101
Li et al. [4]	0.9514193	1.6081636	1.9354025

(a) Bar Diagram view

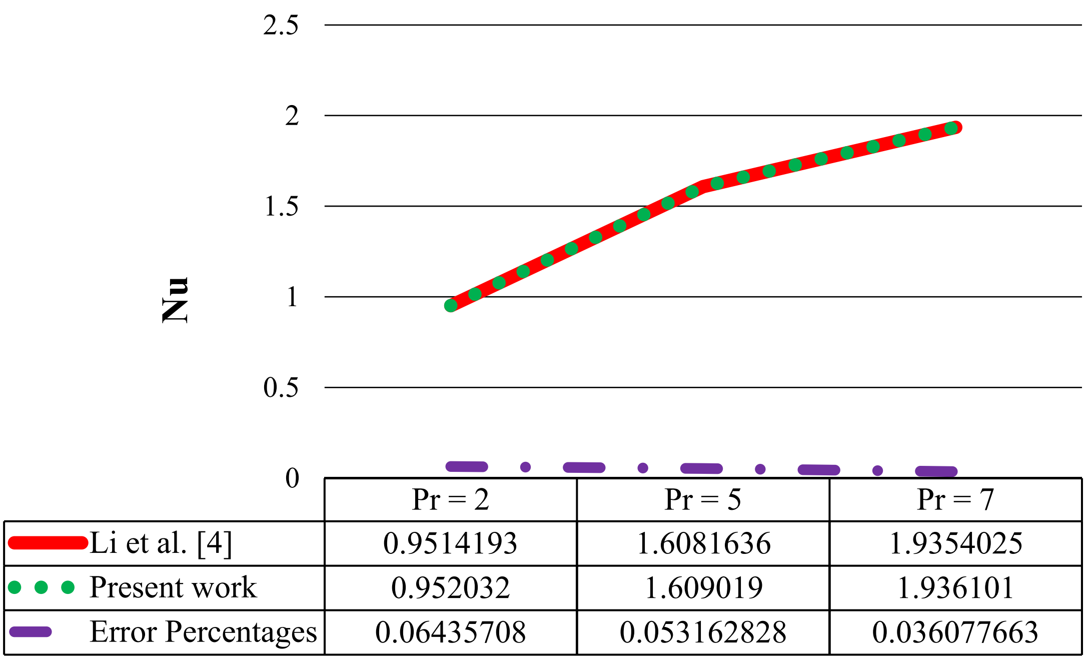

	Pr = 2	Pr = 5	Pr = 7
Li et al. [4]	0.9514193	1.6081636	1.9354025
Present work	0.952032	1.609019	1.936101
Error Percentages	0.06435708	0.053162828	0.036077663

(b) Curves view

Fig. 4. Graphical comparison with Li et al.[4] in (a) Bar Diagram, and (b) Curves.

$$\mathrm{Y}_M = \begin{bmatrix} \mathrm{Y}_1 & 0 & 0 \\ 0 & \mathrm{Y}_5 & 0 \\ 0 & 0 & \mathrm{Y}_8 \end{bmatrix} \tag{25}$$

The eigenvalues associated with the matrix described in equation (25) manifest as $\lambda_1 = \mathrm{Y}_1, \lambda_2 = \mathrm{Y}_5$, and $\lambda_3 = \mathrm{Y}_8$. It is imperative that these numerical values adhere to the stability conditions delineated by equation (26),

$$|\mathrm{Y}_1| \le 1, |\mathrm{Y}_5| \le 1 \text{and} |\mathrm{Y}_8| \le 1 \tag{26}$$

Again, let's examine the provided relations,

$$a = \frac{\Delta\tau}{2}, b = U\frac{\Delta\tau}{\Delta X}, c = |-V|\frac{\Delta\tau}{\Delta Y}, d = 2\frac{\Delta\tau}{(\Delta Y)^2} \tag{27}$$

In this context, *a, b, c*, and *d* represent real and non-negative values. Additionally, considering the fact that the magnitudes of *U* and *V* vary

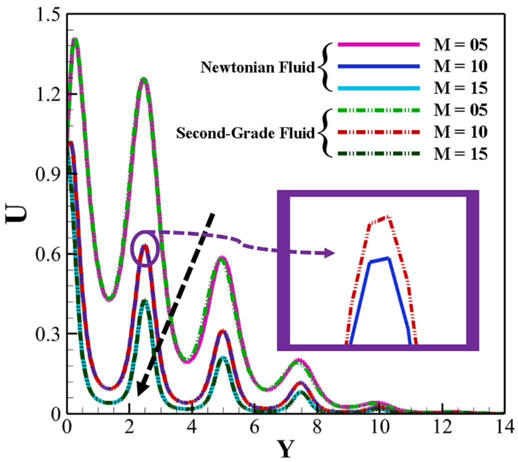

Fig. 5. Velocity profiles vs. magnetic parameter (M) against Y.

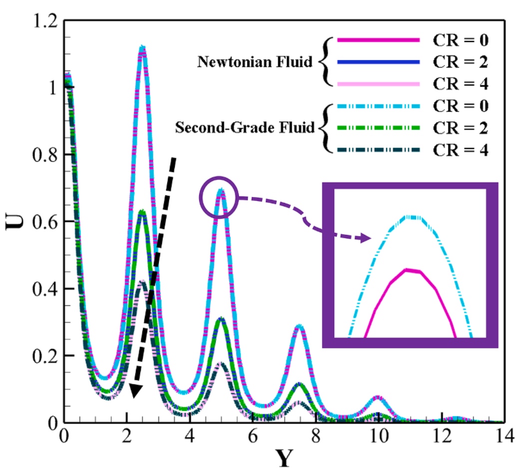

Fig. 6. Velocity profiles vs. chemical reaction (CR) against Y.

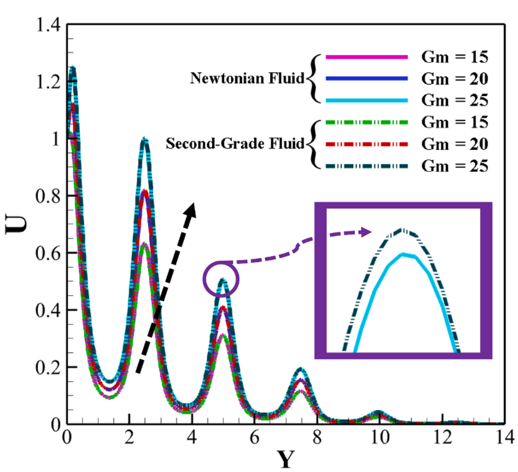

Fig. 7. Velocity profiles vs. mass Grashof number (Gm) against Y.

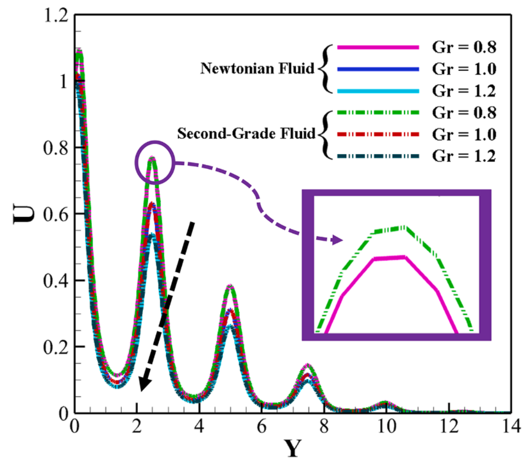

Fig. 8. Velocity profiles vs. thermal Grashof number (Gr) against Y.

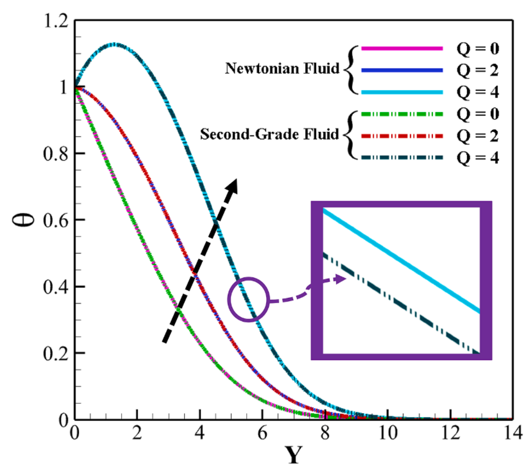

Fig. 9. Temperature profiles vs. heat source parameter (Q) against Y.

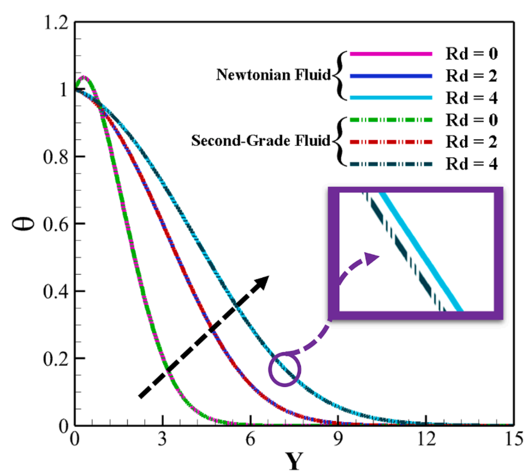

Fig. 10. Temperature profiles vs. radiation parameter (Rd) against Y.

between positive and negative values, progressively. Thus, the highest modulus for $\lambda_1 = \Upsilon_1, \lambda_2 = \Upsilon_5$ and $\lambda_3 = \Upsilon_8$ can be achieved when $\alpha\Delta X = m\pi$ and $\beta\Delta Y = n\pi$ are associated with odd integers m and n. Now, through the utilization of equations (27) in the respective Υ_1, Υ_5 andΥ_8, following equations (28-30) are obtained:

$$\Upsilon_1 = 1 - 2\left\{d + a\alpha + aM^2\sin^2(\pi X) - c + b\right\} - \frac{dSg}{a}(5b + 3c) \tag{28}$$

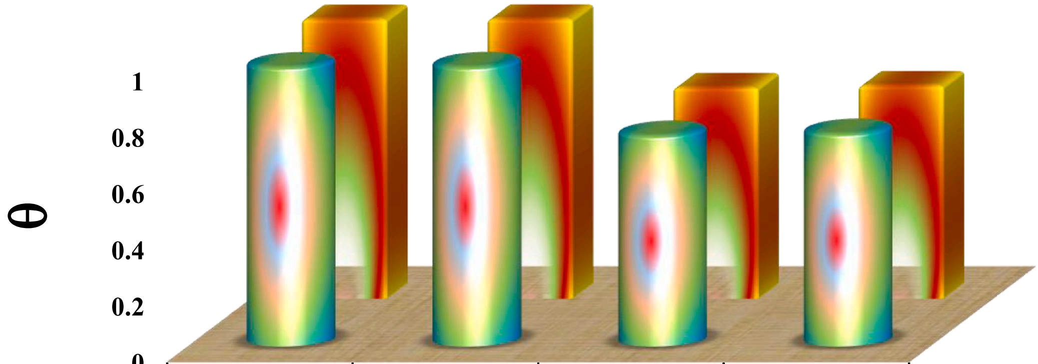

	Y = 0.2		Y = 2.2	
	Nt = 0.3	Nt = 0.5	Nt = 0.3	Nt = 0.5
Newtonian Fluid	0.99335	0.99404	0.75009	0.75685
Second-Grade Fluid	0.99327	0.99397	0.75007	0.75695

Fig. 11. Temperature profiles vs. thermophoresis parameter (Nt) against Y.

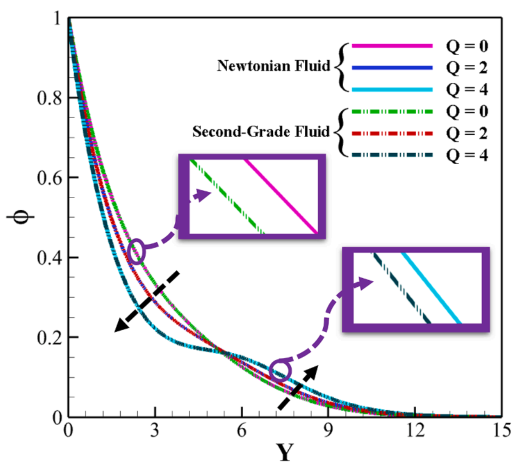

Fig. 12. Concentration profiles vs. heat source parameter (Q) against Y.

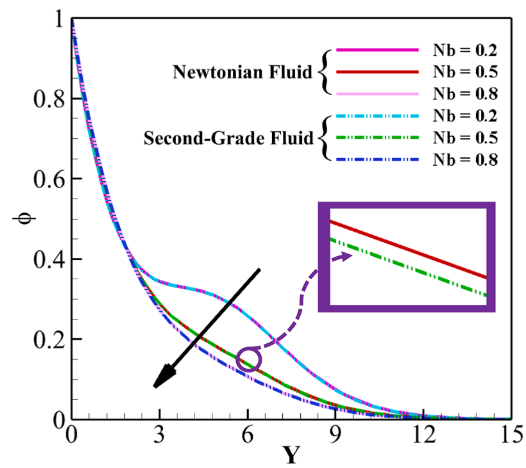

Fig. 14. Concentration profiles vs. Brownian parameter (Nb) against Y.

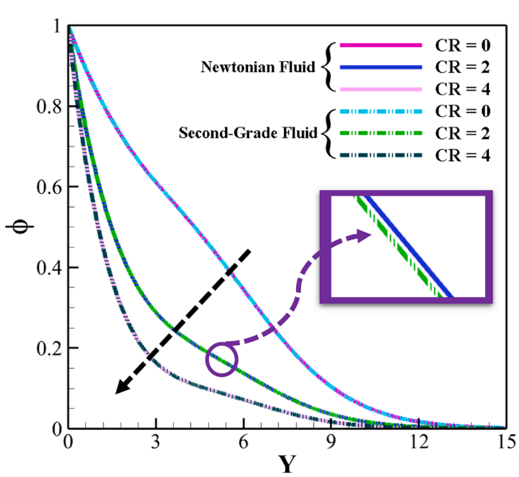

Fig. 13. Concentration profiles vs. chemical reaction parameter (CR) against Y.

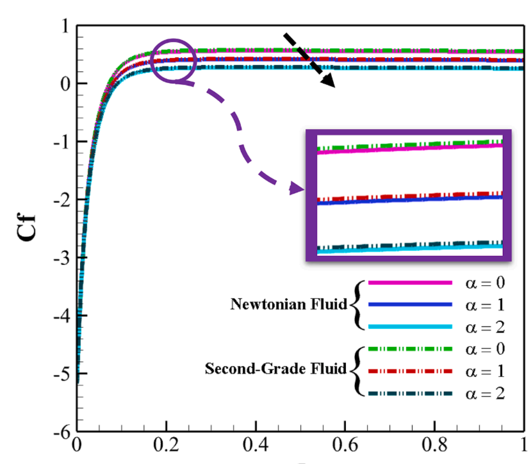

Fig. 15. Skin friction profiles vs. porosity parameter (α) against time (τ).

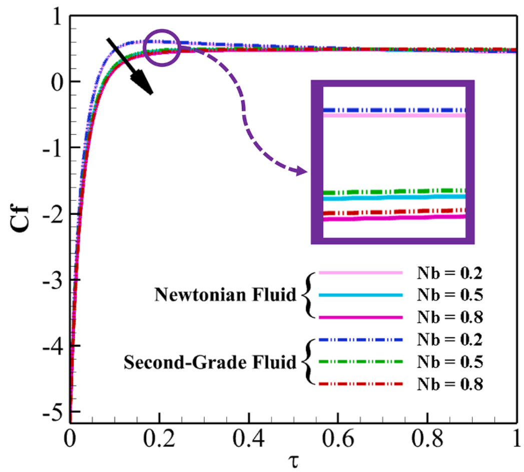

Fig. 16. Skin friction profiles vs. Brownian parameter (*Nb*) against time (τ).

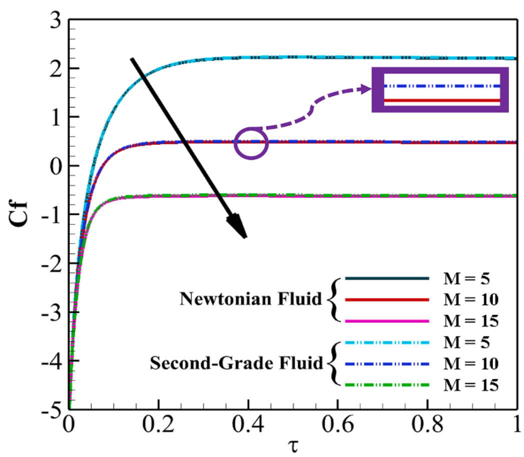

Fig. 17. Skin friction profiles vs. magnetic parameter (*M*) against time (τ).

$$Y_5 = 1 - 2\left[d\frac{1+Rd\{1+(\theta_w-1)\theta\}^3}{\Pr} + c + b - d\left\{Nt\theta + Nb\phi + \frac{Rd\{1+(\theta_w-1)\theta\}^2}{\Pr}\theta\right\}\right] \tag{29}$$

$$Y_8 = 1 - 2\left\{d\frac{1}{Le} + c - b + aCR\right\} \tag{30}$$

Therefore, the numbers $Y_1 = -1$, $Y_5 = -1$ and $Y_8 = -1$ are selected to meet acceptable requirements. Consequently, equations (31), (32), and (33) may be used to represent the stability environment.

$$2\frac{\Delta\tau}{(\Delta Y)^2} + V\frac{\Delta\tau}{\Delta Y} + U\frac{\Delta\tau}{\Delta X} + M^2\sin^2(\pi X)\Delta\tau + \alpha\Delta\tau - \frac{4Sg}{(\Delta Y)^2}\left(5U\frac{\Delta\tau}{\Delta X} + 3V\frac{\Delta\tau}{\Delta Y}\right) \leq 1 \tag{31}$$

$$V\frac{\Delta\tau}{\Delta Y} + U\frac{\Delta\tau}{\Delta X} + 2\frac{\Delta\tau}{(\Delta Y)^2}\left\{\frac{1+Rd\{1+(\theta_w-1)\theta\}^3}{\Pr} + Nt\theta + Nb\phi - \frac{Rd\{1+(\theta_w-1)\theta\}^2}{\Pr}\theta\right\} \leq 1 \tag{32}$$

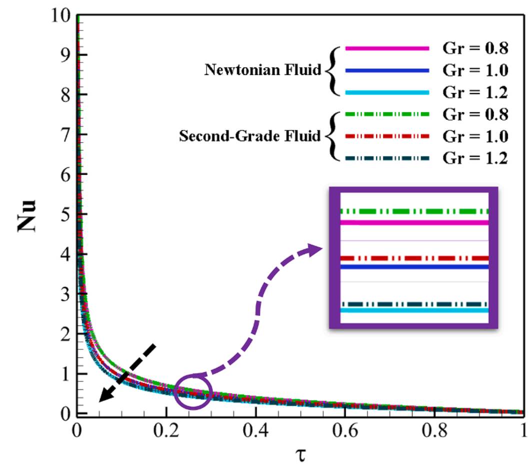

Fig. 18. Nusselt number profiles vs. thermal Grashof number (Gr) against time (τ).

$$2\frac{\Delta\tau}{(\Delta Y)^2}\frac{1}{\Pr Le} + V\frac{\Delta\tau}{\Delta Y} - U\frac{\Delta\tau}{\Delta X} + CR\Delta\tau \leq 1 \tag{33}$$

The convergence criteria for the present investigation will be established concerning $\Pr \geq 0.075$ and $Le \geq 0.035$ under fundamental boundary conditions, as well as for $\Delta\tau = 0.0005$, $\Delta X = 0.08$, and $\Delta Y = 0.2$.

7. Validation

The study conducted by Li et al.[4] is examined for validity and precision using the numerical and graphical comparisons shown in Fig. 4. The Nusselt number in relation to the Prandtl number is the subject of Fig. 4. The most recent findings confirm the earlier findings in the literature and fit in amazingly well with the previously published study.

8. Results and Discussion

In order to examine the modelling complexities involved in periodic magneto hydrodynamics that govern the nonlinear radiative behavior of a second-grade Nano fluid flow emerging from an extended surface that is characterized by the presence of a heat source, the current framework has been used to compare the behavior of the Newtonian fluid and second-grade fluid. When *Pr* is more than 0.075 and Le is equal to or greater than 0.035, convergence is reached. The convergence evaluation in Section 6 requires *Ec* to be maintained at a minimum, ideally nearing insignificance, represented as $Ec << 1$.

In addition, certain particular numbers have been selected to be additional parameters to complement the previously established ones: $Gr = 1.0$, $M = 10.0$, $Gm = 15.0$, $Rd = 2.0$, $Nb = 0.5$, $Nt = 0.3$, $\alpha = 1.0$, $Le = 0.1$, $Ec = 0.05$, $Pr = 0.71$, $CR = 2.0$, $\theta_w = 1.5$, $Q = 1.00$, and $Sg = 0.40$. As a result, a number of fluid dynamics paradigms have been investigated, exploring the complex physical phenomena displayed by several key components, as shown in Figs. 5-25.

8.1. Velocity field

Fig. 5 shows the effect of the magnetic field on the velocity characteristics of Newtonian fluid and second-grade fluid. The picture depicts the effect of the Lorentz force, which functions as a resistive force in magnetic fields and causes a velocity decrease as the magnetic field strength increases. The results reported in reference[54] support this conclusion. It is important to note that the second-grade fluid moves at a lower speed than the Newtonian equivalent. There are several opportunities that arise from this kind of behavior, especially in the area of

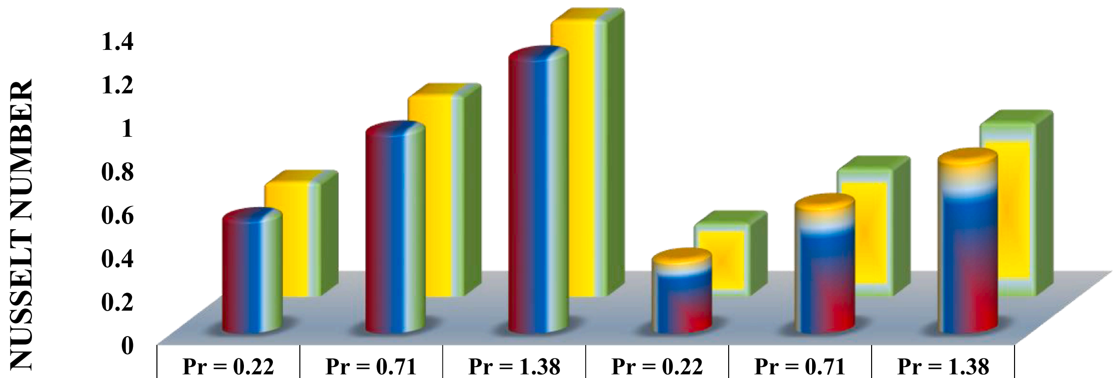

	Pr = 0.22	Pr = 0.71	Pr = 1.38	Pr = 0.22	Pr = 0.71	Pr = 1.38
	Time = 0.1			Time = 0.2		
Newtonian Fluid	0.52554	0.92358	1.26826	0.33912	0.5897	0.7994
Second-Grade Fluid	0.5259	0.92472	1.27041	0.33951	0.59095	0.80173

Fig. 19. Nusselt number profiles vs. Prandtl number (*Pr*) against time (τ).

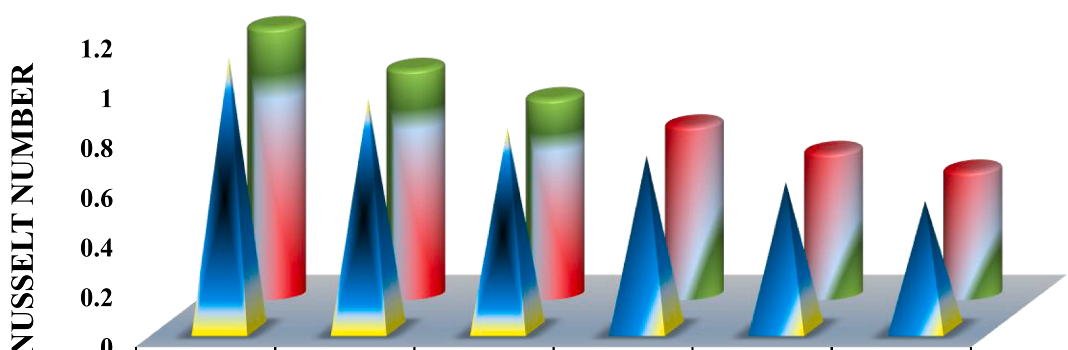

	Gr = 0.8	Gr = 1.0	Gr = 1.2	Gr = 0.8	Gr = 1.0	Gr = 1.2
	Time = 0.1			Time = 0.2		
Newtonian Fluid	1.09082	0.92358	0.806	0.69582	0.5897	0.51492
Second-Grade Fluid	1.09233	0.92472	0.80695	0.69755	0.59095	0.51592

Fig. 20. Nusselt number profiles vs. Grashof number (*Gr*) against time (τ).

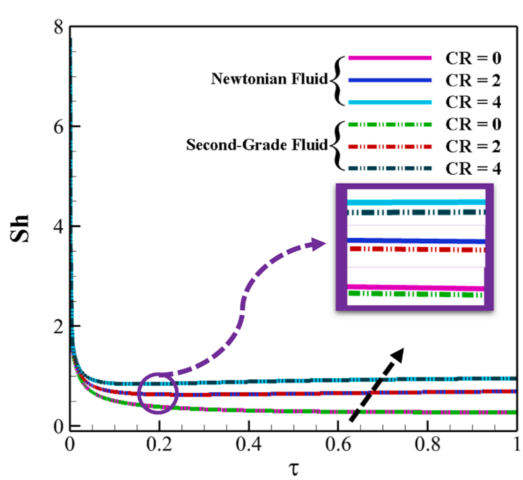

Fig. 21. Sherwood number profiles vs. chemical reaction parameter (*CR*) against time (τ).

dynamic control. A thorough understanding of these phenomena is essential for process optimization in industries where fluid flow is governed by magnetic fields.

As Fig. 6 illustrates, the inclusion of the chemical reaction parameter has a significant effect on the velocity profiles. It is evident that the velocity in both Newtonian and second-grade fluid types reduces with increasing magnetic field intensity. The peculiar behaviour of the velocity profiles of the second-grade fluid, which exhibit an upward trend in contrast to the Newtonian fluid, is intriguing, nevertheless. As has been highlighted in the literature, modifications to the chemical reaction parameter result in considerable modifications to the way that chemical reactions interact with the internal structure of the fluid[3]. As a result, compared to Newtonian fluids, velocity profiles experience more complicated transformations.

When Gr was present, the second-grade fluid's velocity profile was higher than that of the Newtonian fluid, as seen in Fig. 7. The mass Grashof number is a quantitative measure of the relative dominance of buoyant forces over viscous forces in a fluid. It arises from a temperature gradient and has a substantial effect on flows driven by buoyancy and velocity, in accordance with the observations made in the publications[6,7, and 54]. A thorough understanding of the behavior of

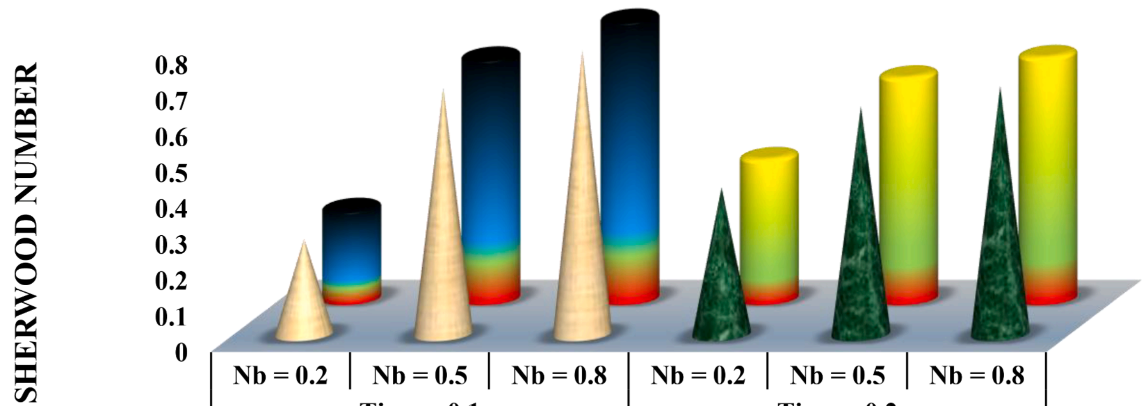

	Nb = 0.2	Nb = 0.5	Nb = 0.8	Nb = 0.2	Nb = 0.5	Nb = 0.8
	Time = 0.1			Time = 0.2		
Newtonian Fluid	0.26565	0.68617	0.79115	0.40751	0.63371	0.69013
Second-Grade Fluid	0.26433	0.68571	0.79094	0.40607	0.63325	0.68993

Fig. 22. Sherwood number profiles vs. Brownian parameter (Nb) against time (τ).

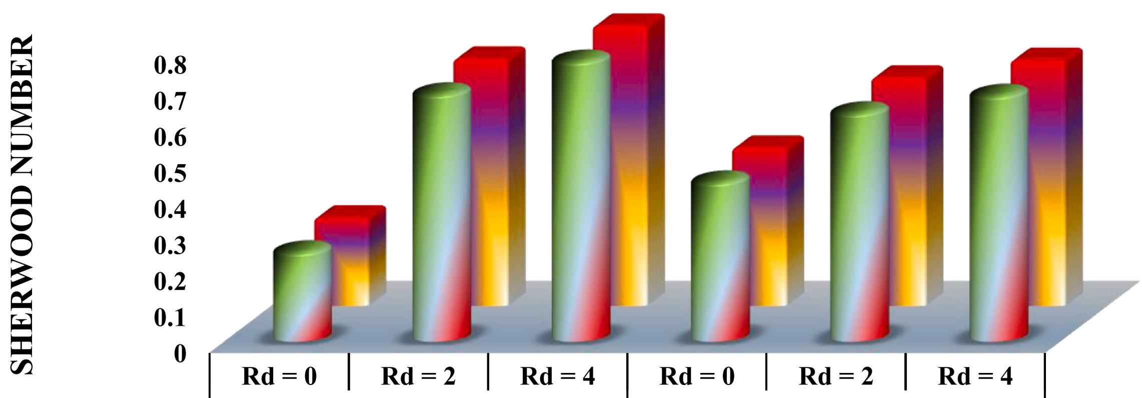

	Rd = 0	Rd = 2	Rd = 4	Rd = 0	Rd = 2	Rd = 4
	Time = 0.1			Time = 0.2		
Newtonian Fluid	0.2486	0.68617	0.7772	0.44231	0.63371	0.68238
Second-Grade Fluid	0.24557	0.68571	0.77705	0.43893	0.63325	0.68223

Fig. 23. Sherwood number profiles vs. Radiation parameter (Rd) against time (τ).

non-Newtonian fluids in response to changes in apparent viscosity is essential for applications ranging from chemical processes to environmental engineering and heat exchanger design. Gaining this understanding is essential to improving flow patterns and maximizing heat transfer effectiveness.

Fig. 8 illustrates a deterioration in the flow characteristics of a non-Newtonian fluid in relation to a Newtonian fluid, as evidenced by the velocity profile in the presence of the thermal Grashof number. As the thermal Grashof number (Gr) increases, both fluid types exhibit a decrease in velocity, as seen in Fig. 8. Extended-chain polymers cause a non-linear rheological response in fluids with second-grade viscosity, which affects the connection with the thermal Grashof number. Changing the thermal Grashof number modifies the way buoyancy forces interact with the fluid's internal structure, which has a more complex effect on velocity profiles than it does for Newtonian fluids[3,6,7,54, and 55]. On the other hand, in circumstances when nuanced and accurate flow characteristics are required, the complex velocity profile patterns in fluids with second-grade features offer potential to customize controlled flows driven by buoyancy.

8.2. Temperature field

The heat source parameter quantifies how much energy or warmth from the outside influences the temperature distribution of the fluid. Within both Newtonian and second-grade fluids, temperature changes become more noticeable as this parameter rises, suggesting increased external heating. Notably, as Fig. 9 illustrates, the rising heat source parameter causes temperature increase in both fluid types. Newtonian fluids have a constant viscosity and a linear connection between shear stress and shear rate, which allow them to react to variations in the heat source parameter. Conversely, because of differences in the heat source parameter, second-grade fluids display intricate temperature patterns, which may be advantageous in applications that need for precise and regulated heating. Understanding the nuanced reactions of second-grade fluids to variations in the heat source parameter is imperative for designing systems with precise temperature regulation, particularly in biomedical applications such as hyperthermia treatment and polymer manufacturing.

The temperature trends that second-grade and Newtonian fluids display with respect to the radiation parameter (Rd) are illustrated in Fig. 10. The radiation parameter plays a major role in the field of heat transfer, especially when thermal radiation is present[54]. A deep

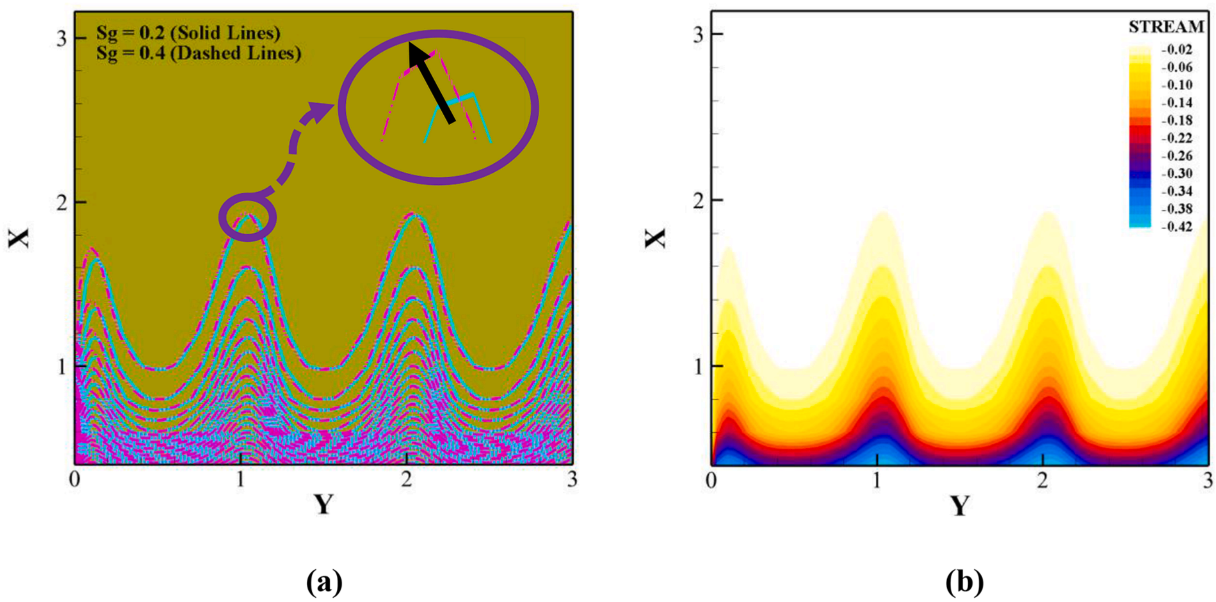

Fig. 24. **(a)** Line view and **(b)** Flood view of stream lines vs. second-grade parameter (Sg).

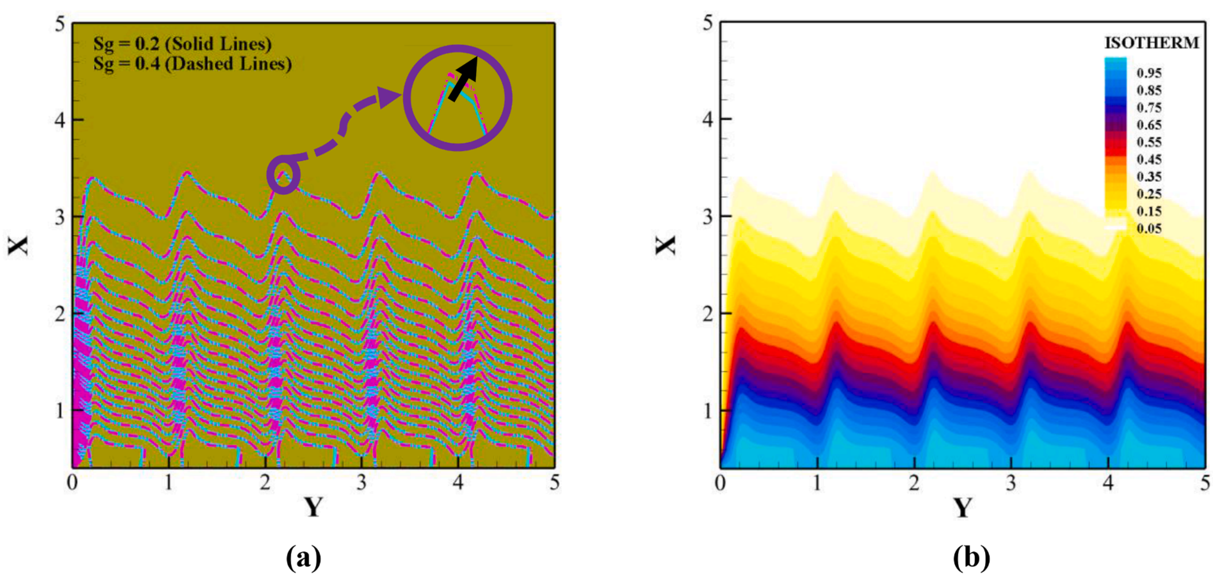

Fig. 25. **(a)** Line view and **(b)** Flood view of isothermal lines vs. second-grade parameter (Sg).

Table 2
Regression statistics of the Nusselt number.

Regression Statistics	
Multiple R	0.999111905
R Square	0.998224599
Adjusted R Square	0.998019745
Standard Error	0.011203919
Observations	30

Table 3
Tabular representation of the correlation of the Nusselt number with different parameters.

Related parameters	*Rd*	*Pr*	*Nt*	*Nusselt Number*
Rd	1			-0.87079
Pr		1		0.628306
Nt			1	0.167087

knowledge of the response of second-grade and Newtonian fluids to perturbations in the radiation parameter is essential for practical applications, particularly in sectors such as the energy industry. As the radiation parameter increases, temperature differences become more pronounced, indicating a higher frequency of radiative heat transfer. As a result, temperature upsurges as the radiation parameter growths, despite the fact that Newtonian fluids are naturally hotter than second-grade fluids.

Temperature changes in second-grade and Newtonian fluids with respect to *Nt* are explained in Fig. 11. Both fluid types show temperature increase with a rising thermophoresis parameter, despite the fact that Newtonian fluids have an intrinsically greater temperature. Fluid temperature distribution is greatly influenced by thermophoresis, which is the movement of particles in response to temperature gradients. Higher temperatures are naturally maintained by Newtonian fluids, which are

Table 4
Tabular representation of predicted values, obtained values, and residual values.

Observation	*Obtained Nusselt Number*	*Predicted Nusselt Number*	*Residuals*
1	0.62528	0.623641757	0.001638243
2	0.59095	0.568313376	0.022636624
3	0.51425	0.512984994	0.001265006
4	0.45874	0.457656613	0.001083387
5	0.40322	0.402328231	0.000891769
6	0.34771	0.34699985	0.00071015
7	0.29219	0.291671468	0.000518532
8	0.23668	0.236343087	0.000336913
9	0.18116	0.181014705	0.000145295
10	0.12565	0.125686324	-3.63237E-05
11	0.07013	0.070357942	-0.000227942
12	0.01462	0.015029561	-0.000409561
13	-0.04089	-0.040298821	-0.000591179
14	0.33951	0.376978374	-0.037468374
15	0.53862	0.537075008	0.001544992
16	0.59095	0.568313376	0.022636624
17	0.68267	0.681552458	0.001117542
18	0.80173	0.829934704	-0.028204704
19	0.91628	0.915840215	0.000439785
20	1.07199	1.072032053	-4.20528E-05
21	0.56645	0.562455298	0.003994702
22	0.56791	0.565384337	0.002525663
23	0.56976	0.568313376	0.001446624
24	0.57247	0.571242414	0.001227586
25	0.57515	0.574171453	0.000978547
26	0.57789	0.577100492	0.000789508
27	0.58058	0.58002953	0.00055047
28	0.583285	0.582958569	0.000326431
29	0.58599	0.585887608	0.000102392
30	0.58889	0.588816646	7.33536E-05

defined by their viscosity and the link between shear stress and shear rate. The complex temperature swings in second-grade fluids with a non-linear rheological response are a result of the interaction between the thermophoresis parameter and internal fluid structure. Particle mobility alters when the thermophoresis parameter increases, influencing heat transmission and raising the temperature as a result. These observations have real-world implications in the chemical engineering and environmental domains, where those are used to optimize heat exchanger designs and enhance thermal process efficiency.

8.3. Concentration field

The concentration profiles of Newtonian and second-grade fluids with respect to the heat source parameter (Q) are shown in Fig. 12. While second-grade fluids and Newtonian fluids have larger concentrations by nature, both show a decrease in concentration when the heat source parameter increases in the interval ($0 < Y < 5.5$) and an opposite tendency outside of this range ($Y > 5.5$). Particles are first driven from the hotter center area to the cooler peripheral portions by thermal diffusion, which results in a drop in concentration. A concentration boundary layer develops beyond $Y = 5.5$, where particle diffusion is encouraged by the higher heat source value. In this area, heat and mass transfer work together to affect concentration gradients. Thermal diffusion is responsible for the first decrease in concentration. As the heat source parameter increases, buoyancy-induced flow and improved convective transport are probably responsible for the second increase in concentration. When temperature changes impact second-grade fluids, the non-linear stress-strain relationship leads to increasingly intricate flow patterns. These fluids exhibit decreased viscosity and increasing flow rates as temperatures rise, resulting in a variety of concentration distributions in various locations. This demonstrates the complex relationship between fluid characteristics and thermal impacts, pointing to creative ways to improve conditions and product quality in operations involving heat-sensitive materials, such chemical synthesis and material processing.

Concentration patterns with respect to the chemical reaction parameter (*CR*) are shown in Fig. 13 for Newtonian and second-grade fluids. The interesting thing is that both show a concentration fall with increasing chemical reaction parameter, even though Newtonian fluids have larger concentrations by nature. A universal decrease in concentration occurs for both Newtonian and second-grade fluids when the chemical reaction parameter is raised, causing modifications in the fluid's molecular interactions and composition. This illustrates how the chemical reaction parameter affects the dynamics of concentration in a broad way. Through informed control of chemical processes, this information may be used to a variety of sectors, such as chemical engineering, pharmaceuticals, and material sciences, to optimize reaction conditions and improve product quality.

Concentration patterns for the Brownian parameter (*Nb*) in Newtonian and second-grade fluids are shown in Fig. 14. Even if the first stages of both fluids' concentrations are slightly greater, an inverse tendency is seen later on. Concentration decreases in both cases as the Brownian parameter increases. Newtonian fluids have a larger concentration than second-grade fluids at a particular place, but Brownian motion more obviously enhances particle dispersion in second-grade fluids. A greater dispersion and mobility of particles in the fluids is suggested by the overall concentration falling as the Brownian parameter increases. This insight has uses in the fields of nanotechnology, colloidal systems, and pharmaceuticals. It makes it possible to intelligently control the qualities of materials, enhancing product quality and maximizing the environment for desired particle behaviors.

8.4. Skin friction

Through line profiles, Fig. 15 examines the skin friction properties of Newtonian and second-grade fluids, paying particular attention to variations in the porosity parameter (α). The ratio of empty spaces in a porous material is measured by the porosity parameter, which has an immediate effect on the parameters of fluid flow. When a result, skin friction decreases when porosity parameters rise, which is consistent with findings from previous studies[6,54, and 55]. Furthermore, it is found that second-grade fluid has skin friction that is higher than that of Newtonian fluid. Comprehending the behavior of these fluids with respect to changes in the porosity parameter is essential for the effective use of porous media flow, particularly in settings like filtration systems, geological operations, and biomedical apparatus. Fig. 16 illustrates skin friction characteristics in second-grade and Newtonian fluids, focusing on changes in the Brownian parameter (*Nb*). There is a discernible pattern wherein skin friction lowers for both fluids as the values of the Brownian parameter rise, even if the skin friction of the second-grade fluid is somewhat larger than that of the Newtonian fluid. Greater random particle motion is induced by the larger Brownian parameter, which helps to lessen skin friction and encourage more fluid flow. The consistent pattern of decreasing skin friction with rising values of the Brownian parameter, even if the skin friction of the second-grade fluid is somewhat higher than that of the Newtonian fluid, highlights the critical function of Brownian motion in modifying the frictional forces inside the fluids. This common pattern offers important design insights for systems where friction control is essential, especially in modern manufacturing processes and biomedical applications.

The skin friction properties of second-grade and Newtonian fluids are examined in Fig. 17, with particular attention to changes in the magnetic parameter (M). The observed trend shows that for both fluids, skin friction reduces as the magnetic parameter increases. It is noteworthy that the second-grade fluid exhibits somewhat greater skin friction than the Newtonian fluid. Higher magnetic parameters result in the application of magnetic forces to the fluid, hence promoting smoother fluid flow and reducing skin friction. This makes sense given the principles of magnetic field theory (MHD), which explains how magnetic fields impact electrically conducting fluids. Even though the skin friction of the second-grade fluid increased somewhat, the overall trend highlights

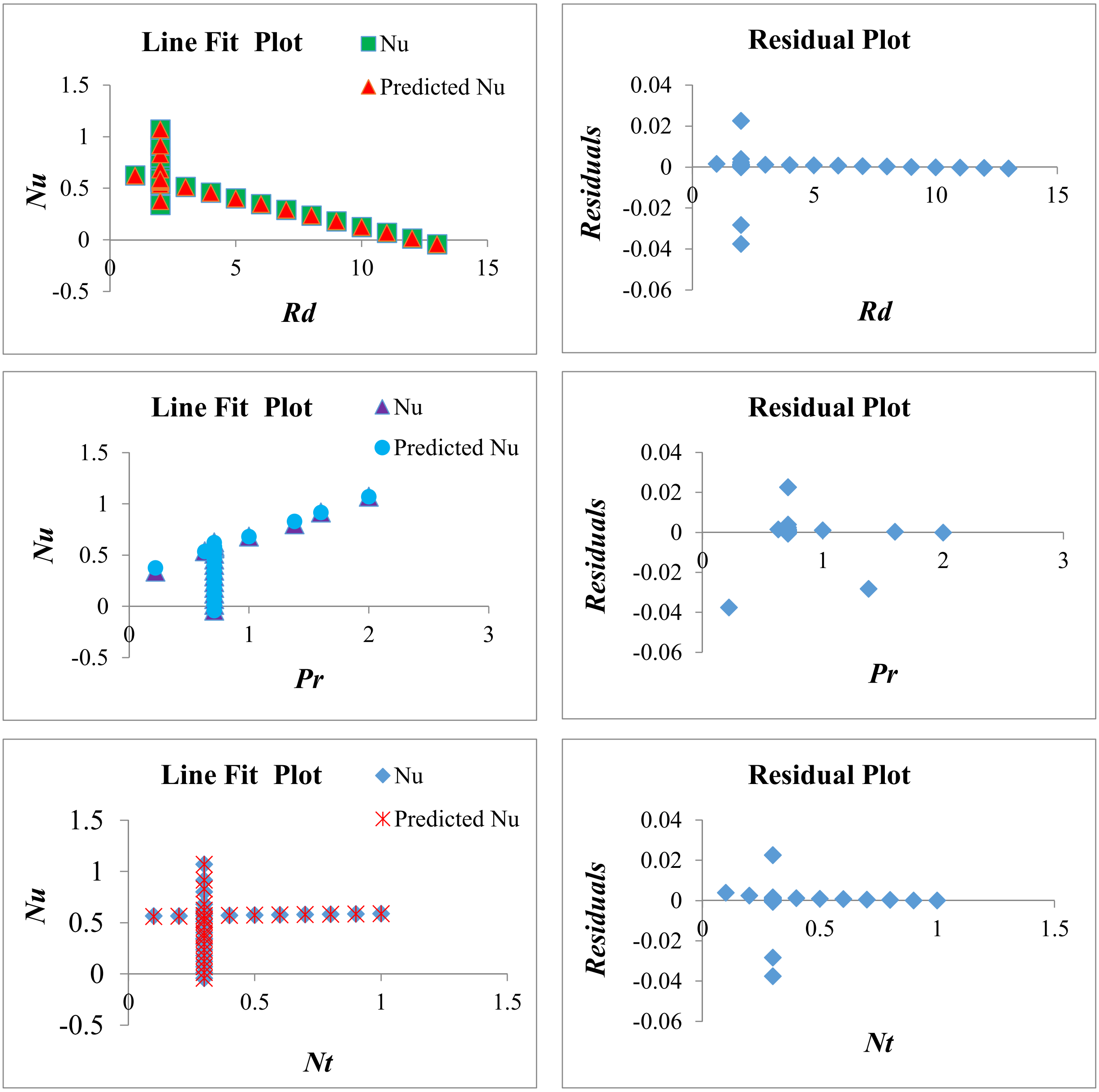

Fig. 26. Plots for obtained vs. predicted values of the Nusselt number for different parameters with residual plots.

Table 5
Regression statistics of the Sherwood number.

Regression Statistics	
Multiple R	0.999958467
R Square	0.999916936
Adjusted R Square	0.999907352
Standard Error	0.002632386
Observations	30

Table 6
Tabular representation of the correlation of the Sherwood number with different parameters.

Related parameters	*Nb*	*CR*	*Gm*	Sherwood *Number*
Nb	1			0.566721
CR		1		0.922131
Gm			1	0.087072

the important role that magnetic forces play in changing the frictional forces in the fluids. This information may be used by sectors such as industrial pipeline flow management, microfluidic systems, and magnetic drug targeting to improve overall efficiency and optimize conditions.

8.5. Nusselt number

Fig. 18 shows the Nusselt number trend for the Newtonian and second-grade fluids. The second-grade fluid shows a larger drop than the Newtonian fluid. The relationship between buoyant forces and internal fluid composition varies as the thermal Grashof number does. This effect on Nusselt numbers is less significant than for Newtonian fluids, as the following articles[2,6,45, and 55] also demonstrate. In sectors where natural convection heat transfer is important and precise regulation of Nusselt number profiles is required, these characteristics are critical to optimum efficiency.

Fig. 19 illustrates the Nusselt number trends for both Newtonian and second-grade fluids. Notably, the second-grade fluid displays a more

Table 7
Tabular representation of predicted values, obtained values, and residual values.

Observation	*Obtained Sherwood Number*	*Predicted Sherwood Number*	*Residuals*
1	0.54284	0.543297482	-0.00045748
2	0.56385	0.564288393	-0.00043839
3	0.584866	0.585279303	-0.00041330
4	0.60587	0.606270214	-0.00040021
5	0.63325	0.627261124	0.00598887
6	0.6479	0.648252034	-0.00035203
7	0.66891	0.669242945	-0.00033294
8	0.68993	0.690233855	-0.00030385
9	0.71094	0.711224765	-0.00028476
10	0.731955	0.732215676	-0.00026067
11	0.51175	0.512286291	-0.00053629
12	0.63325	0.627261124	0.00598887
13	0.74209	0.742235956	-0.00014595
14	0.847	0.857210789	-0.01021078
15	0.9723	0.972185621	0.00011437
16	1.08744	1.087160454	0.00027954
17	1.20257	1.202135286	0.00043471
18	1.31771	1.317110119	0.00059988
19	1.43285	1.432084951	0.00076504
20	1.54799	1.547059784	0.00093021
21	0.62689	0.627261124	-0.00037112
22	0.62778	0.628101648	-0.00032164
23	0.62867	0.628942173	-0.00027217
24	0.62956	0.629782697	-0.00022269
25	0.63045	0.630623221	-0.00017322
26	0.63186	0.631463745	0.00039625
27	0.63223	0.63230427	-7.42697E-0
28	0.63312	0.633144794	-2.4794E-05
29	0.63401	0.633985318	2.46817E-05
30	0.6349	0.634825843	7.41574E-05

increased compared to the Newtonian fluid. Moreover, increased values of the Prandtl number are observed to correlate with an increase in the Nusselt number in both Newtonian and second-grade fluid flows. Compared to the Newtonian fluid, the second-grade fluid's Nusselt number trend has a steeper slope, suggesting a more effective heat transfer mechanism that is probably affected by its unique rheological properties and non-linear response. A larger Prandtl number indicates that momentum diffusion predominates over thermal diffusion, which improves convective heat transfer a useful property in situations where efficient heat transfer is necessary.

The bar plot depicted in Fig. 20 outlines the Nusselt number trends in relation to the Grashof number for both Newtonian and second-grade fluids. Notably, the second-grade fluid displays a more notable increase in comparison to the Newtonian fluid. Furthermore, it is important to highlight that, in the context of both Newtonian and second-grade fluid flows, higher values of the Grashof number correspond to lower values of the Nusselt number. The unique rheological attributes of the second-grade fluid are likely responsible for the notable elevation in its Nusselt number, with its non-linear response, setting it apart from the Newtonian fluid, potentially contributing to enhanced convective heat transfer characteristics. Higher Grashof numbers indicate more buoyant forces, which lead to less convective heat transfer a feature that is observed in both Newtonian and second-grade fluids. Significant rise in the second-grade fluid suggests possible advantages in situations needing increased heat transmission, as in thermal management systems or cooling operations.

8.6. *Sherwood number*

The complicated interactions between the chemical reaction parameter and second-grade fluids are influenced by non-linear rheological behavior, which is commonly observed in the presence of long-chain polymers. The relationship between chemical reactions and the internal structure of the fluid is affected by changes in the chemical reaction parameter in a more complex manner than it is in fluids of lower classes. Consequently, data from research papers[3,8, and 54] shows that the Sherwood profile's effect is steadily growing, as demonstrated in Fig. 21. Understanding these dynamics is essential to enhancing performance in sectors where mass transfer efficiency must be strictly controlled and chemical reactions play a significant role.

For both Newtonian and second-grade fluids, the reaction of the Sherwood number to changes in the Brownian parameter is depicted in the bar diagram in Fig. 22. It is noteworthy that in both fluid flows, the Sherwood number increases as the values of the Brownian parameter climb. Significantly, the Newtonian fluid's Sherwood number is higher than the fluid's second-grade value. The random mobility of particles inside the fluid increases as the Brownian parameter grows, improving the efficiency of mass transfer. The non-linear rheological response of the second-grade fluid is in contrast to the mass transfer qualities of the Newtonian fluid, which is defined by linear viscosity. This knowledge may be used by industries like chemical engineering and environmental applications, which operate in processes where mass transfer efficiency is critical, to optimize conditions.

The bar diagram in Fig. 23 shows how the Sherwood number changes for both second-grade and Newtonian fluids in response to changes in the radiation parameter. Notably, it is shown that when the radiation parameter rises, the Sherwood number increases in both fluid flows. It is noteworthy that the Newtonian fluid's Sherwood number is higher than the fluid's second-grade one. Thermal radiation becomes more intense as the radiation parameter rises, which improves mass transfer efficiency by facilitating better heat transmission. Their different rheological behaviors are related to the difference in Sherwood numbers between the Newtonian and second-grade fluids. It is useful to compare Newtonian and second-grade fluids when building systems with specific mass transfer needs.

8.7. *Stream lines and Isothermal lines*

Fig. 24 displays streamlines in both line and flood views, showing a discernible rise in streamlines as the second-grade parameter values rise. The internal structure of the fluid is influenced by the second-grade parameter, which affects the fluid's resistance to deformation and flow. The fluid becomes more resistant to deformation as the second-grade parameter rises, creating a more organized and complicated flow field with a greater streamline density. This information may be utilized in the design and optimization of fluid-flowing systems, such as the creation of effective mixing devices, pipelines, and other fluid-based operations.

There is a discernible rise in the number of isothermal lines as the values of the second-grade parameter rise in Fig. 25, which shows the isothermal lines from both the line and flood views. The fluid's nonlinear rheological reaction is expected to result in a more complex temperature distribution inside the system as the second-grade parameter increases. The fluid's internal structure and thermal conductivity are influenced by the second-grade parameter, which affects the fluid's ability to transport heat. Higher second-grade characteristics are linked to more isothermal lines, which may present chances for improving thermal efficiency and heat transmission in a variety of systems and processes.

8.8. *Regression, correlation and data prediction of Nusselt number*

When it comes to heat transfer rate analysis, the Nusselt number (Nu) is the primary dependent variable. Pr, Nt, and Rd all operate simultaneously as separate factors within this intricate interaction. The following linear equation provides a succinct representation of the complex relationships between these variables:

$$Nu = 0.39294 - 0.05533Rd + 0.39048\mathrm{Pr} + 0.02929Nt$$

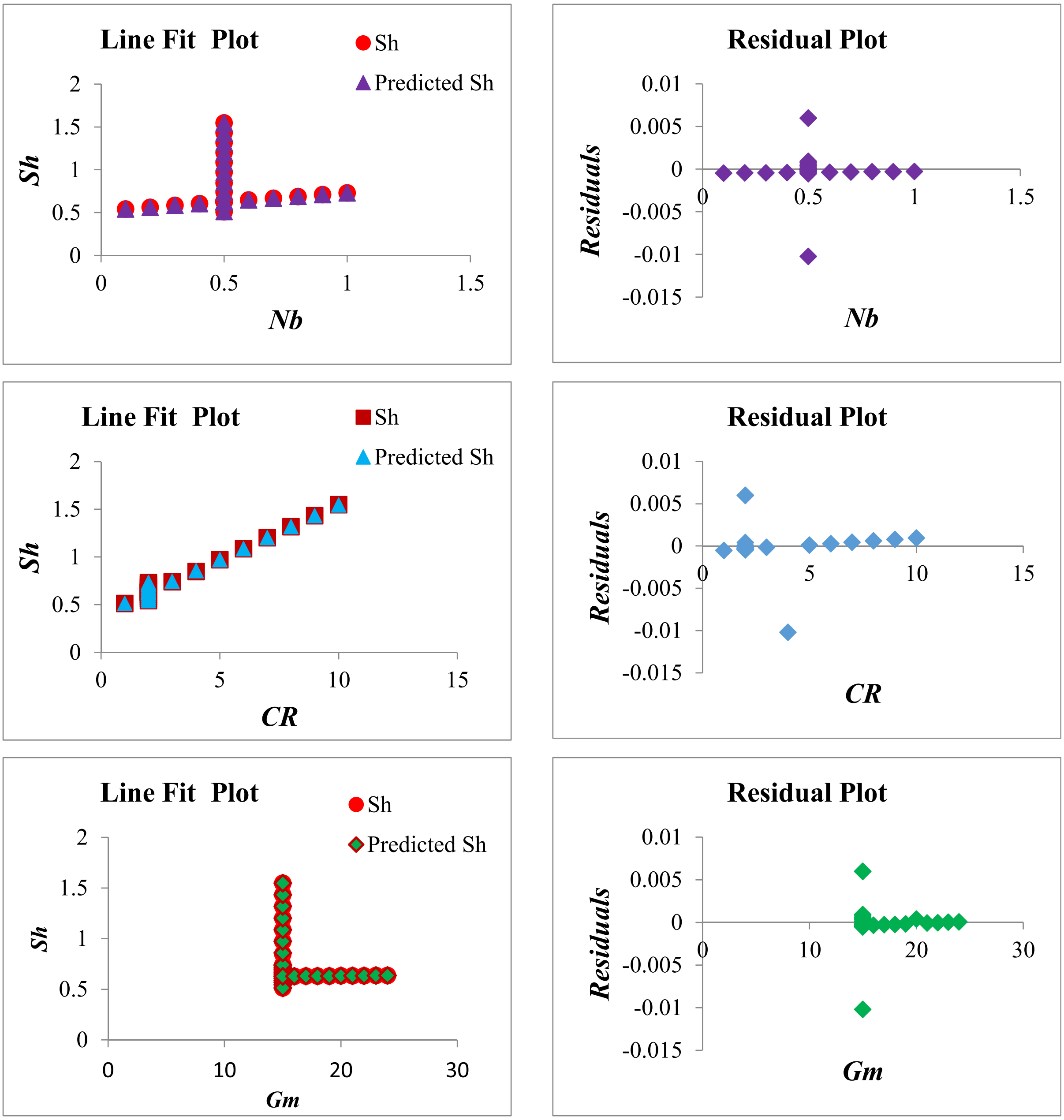

Fig. 27. Plots for obtained vs. predicted values of the Sherwood number for different parameters with residual plots.

The statistical analysis has shown the usefulness and robustness of the equation at a 95% confidence level. This is really important. With a correlation value (R^2) of 99.82%, the model provides strong support for the validity and strength of the interdependent interactions between the variables in the thermal transmission frameworks. Table 2 painstakingly presents a detailed analysis of these elements.

The findings of the investigation into the correlation between the other parameters and the Nusselt number are shown in Table 3. The idea that there is a significant association between the Nusselt number and the Prandtl number is supported by Table 3, which shows unique correlations between various parameters. The radiation factor, for instance, decreased the Nusselt number while the Prandtl number and thermophoresis increased it, even though the Nusselt number has an inverse correlation with some other parameters. Additionally, as Table 3 shows, *Rd* and *Pr* have a substantial correlation with the Nusselt number, but there is less of a correlation between the Nusselt number and *Nt*. In addition, a table that shows the differences between the study's residuals, expected values, and actual values is provided. Table 4 goes into detail about this information.

Fig. 26 presents six subplots that together offer an in-depth analysis of the Nusselt number. Real values, predicted values, and residual plots over a range of parameters are all included in the analysis. There is a strong agreement between the measured and predicted values, together with low residuals, suggesting that the predictive model is effective at describing underlying physical events in a variety of settings. A high degree of precision in calculating the Nusselt number is implied by the striking closeness between the actual and anticipated values. Model validation is supported by parametric residual plots, which consistently show minimal residuals and show the accuracy and reliability of the model. All things considered, the agreement between the observed and anticipated values validates the accuracy and reliability of the model, confirming its capacity to estimate the Nusselt number under a variety of conditions.

8.9. Regression, correlation and data prediction of Sherwood number

The dependent variable, the Sherwood number (*Sh*), is the main focus of the thermal transmission rate investigation. At the same time, *Nb, CR*, and *Gm* function as the independent variables in this complex interaction. The complex interactions between these variables are concisely represented by the following linear equation:

$$Sh = 0.27974 + 0.20991Nb + 0.11497\mathrm{CR} + 0.00084Gm$$

Based on a 95% confidence level statistical analysis, the study has shown the equation's robustness and usefulness. This is interesting to note. The model's precision and strength of the interdependent interactions among the variables inside the thermal transmission frameworks are well supported by the data, as evidenced by its correlation value (R^2) of 99.99%. Table 5 has an extensive analysis of it.

Table 6 presents the research findings on the relationship between the Sherwood number and other characteristics. This table illustrates several relationships between various factors, confirming a strong correlation between the chemical reaction parameter and the Sherwood number. On the other hand, the connection between the Sherwood number and the Brownian parameter is much less than the Sherwood-mass Grashof number association, even if it is weaker than the Sherwood-chemical reaction correlation. Furthermore, it is interesting that the Sherwood number and the parameters *Nb, CR,* and *Gm* exhibit a positive association, suggesting that the values of the Sherwood number are elevated as a result of these variables.

Additionally, a tabular depiction of the residuals, predicted values, and actual values related to the Sherwood number is provided in Table 7.

Six subplots are used to depict a complex analysis of the Sherwood number in Fig. 27. Real values, projected values, and parametric residual plots over a range of parameters are all included in the analysis. A high degree of agreement between observed and predicted values and low residuals indicate that the predictive model is effective in understanding basic physical processes in a variety of settings. A high degree of precision in calculating the Sherwood number is implied by the striking closeness between the actual and anticipated values. In order to confirm the model's accuracy and dependability, parametric residual plots are utilized, which consistently provide minimal residuals. In general, the agreement between observed and anticipated values validates the accuracy and stability of the model, hence endorsing its suitability for estimating the Sherwood number under a range of conditions and characteristics.

9. Conclusions

Using a non-linear radiative model, this research compares the properties of second-grade and Newtonian fluid flow on a stretched vertical surface with sinusoidal magnetic force. Numerical solutions to non-dimensional equations are obtained by the explicit finite difference technique combined with the FORTRAN platform. To assess the collected data, regression and correlation analysis were performed. These are the key conclusions that were discovered:

- ➢ The velocity profiles indicate a negative association with growing the values of magnetic parameter, thermal Grashof number, and chemical reaction parameter, but a positive correlation with rising mass Grashof number. In addition, the velocity of second-grade fluid flow is 0.68% greater than that of Newtonian fluid flow.
- ➢ Growing factors that lead to rising temperature profiles include thermophoresis, radiation, and heat source. Additionally, as compared to base fluid, the temperature profiles of Newtonian fluid are 0.27% greater than those of second-grade fluid.
- ➢ While concentration profiles exhibit a positive correlation with increasing Brownian parameters and a negative link with expanding values of the chemical reaction parameter, rising heat source parameter displays both positive and negative correlations. Furthermore, second-grade fluid flow is less concentrated than Newtonian fluid flow.
- ➢ Gradual variations in the porosity, Brownian, and magnetic parameters lead to a corresponding decrease in skin friction; additionally, the Nusselt number shows a decrease with a high thermal Grashof number and an increase with the Prandtl number; higher radiation, Brownian, and chemical reaction parameter values result in an increase with the Sherwood number. Furthermore, second-grade fluid flow shows a lower mass transmission rate but a greater stress sharing and heat transmission rate compared to Newtonian fluid flow.
- ➢ As the second-grade parameter experiences an elevation, both the streamlines and isothermal lines exhibit an augmentation.
- ➢ For both phenomena (Sherwood number and Nusselt number), the obtained and predicted values are almost same; moreover, the correlation (R^2) value of the Sherwood number is 99.99% and the correlation (R^2) value of the Nusselt number is 99.82% at a 95% confidence level. Similarly, the residuals for both phenomena are negligible.

These results have important implications for flow characteristic optimization in molding, extrusion, and other production processes. By filling up important information gaps about the interaction between sinusoidal magneto hydrodynamics (MHD) and nonlinear radiation, this research will facilitate the development of more effective design techniques in the fields of engineering, food industry, pharmaceuticals, and thermal sciences. By using artificial neural network (ANN) model analysis on exponentially inclined and stretched surfaces, future study might build on these discoveries even further. Furthermore, an interesting line of inquiry is to investigate the structure and content of nanoparticles.

Declaration of competing interest

The authors declare that they have no known competing financial interests or personal relationships that could have appeared to influence the work reported in this paper.

Data availability

The data that has been used is confidential.

Acknowledgements

The authors express gratitude for the financial support extended by the Research and Innovation Centre, Khulna University, Khulna- 9208, Bangladesh.

References

1. Hayat T, Khan SA, Khan MI, Alsaedi A. Optimizing the theoretical analysis of entropy generation in the flow of second grade nanofluid. *Phys. Scr.* 2019;94(8), 085001.
2. Hayat T, Khan WA, Abbas SZ, Nadeem S, Ahmad S. Impact of induced magnetic field on second-grade nanofluid flow past a convectively heated stretching sheet. *Appl. Nanosci.* 2020;10:3001–3009.
3. Shafiq A, Rasool G, Khalique CM, Aslam S. Second grade bioconvective nanofluid flow with buoyancy effect and chemical reaction. *Symmetry*. 2020;12(4):621.
4. Li Y, Waqas H, Imran M, Farooq U, Mallawi F, Tlili I. A numerical exploration of modified second-grade nanofluid with motile microorganisms, thermal radiation, and Wu's slip. *Symmetry*. 2020;12(3):393.
5. Kalaivanan R, Ganesh NV, Al-Mdallal QM. An investigation on Arrhenius activation energy of second grade nanofluid flow with active and passive control of nanomaterials, Case Stud. *Therm. Eng.* 2020;22, 100774.
6. Jamshed W, Nisar KS, Gowda RP, Kumar RN, Prasannakumara BC. Radiative heat transfer of second grade nanofluid flow past a porous flat surface: a single-phase mathematical model. *Phys. Scr.* 2021;96(6), 064006.

7. Khan SU, Tlili I, Waqas H, Imran M. Effects of nonlinear thermal radiation and activation energy on modified second-grade nanofluid with Cattaneo–Christov expressions. *J. Therm. Anal. Calorim.* 2021;143:1175–1186.
8. Nadeem M, Siddique I, Awrejcewicz J, Bilal M. Numerical analysis of a second-grade fuzzy hybrid nanofluid flow and heat transfer over a permeable stretching/shrinking sheet. *Sci. Rep.* 2022;12(1):1631.
9. Sunthrayuth P, Abdelmohsen SA, Rekha MB, Raghunatha KR, Abdelbacki AM, Gorji MR, Prasannakumara BC. Impact of nanoparticle aggregation on heat transfer phenomena of second grade nanofluid flow over melting surface subject to homogeneous-heterogeneous reactions, Case Stud. *Therm. Eng.* 2022;32, 101897.
10. Basit A, Asjad MI, Akgül A. Convective flow of a fractional second grade fluid containing different nanoparticles with Prabhakar fractional derivative subject to non-uniform velocity at the boundary. *Math. Methods Appl. Sci.* 2023;46(7): 8148–8159.
11. Bayareh M, Usefian A, Nadooshan AA. Rapid mixing of Newtonian and non-Newtonian fluids in a three-dimensional micro-mixer using non-uniform magnetic field. *Int. J. Heat Mass Transf.* 2019;6(1):55–61.
12. Pishkar I, Ghasemi B, Raisi A, Aminossadati SM. Numerical study of unsteady natural convection heat transfer of Newtonian and non-Newtonian fluids in a square enclosure under oscillating heat flux. *J. Therm. Anal. Calorim.* 2019;138:1697–1710.
13. Tseng HC. A revisitation of generalized Newtonian fluids. *J. Rheol.* 2020;64(3): 493–504.
14. Jaszczur M, Młynarczykowska A, Demurtas L. Effect of impeller design on power characteristics and Newtonian fluids mixing efficiency in a mechanically agitated vessel at low Reynolds numbers. *Energies*. 2020;13(3):640.
15. de Goede TC, Moqaddam AM, Limpens KCM, Kooij SA, Derome D, Carmeliet J, Shahidzadeh N, Bonn D. Droplet impact of Newtonian fluids and blood on simple fabrics: Effect of fabric pore size and underlying substrate. *Phys. Fluids.* 2021;33(3).
16. Kumar G, Mondal PK. Application of artificial neural network for understanding multi-layer microscale transport comprising of alternate Newtonian and non-Newtonian fluids. *Colloids Surf. A: Physicochem. Eng. Asp.* 2022;642, 128664.
17. Arosemena AA, Andersson HI, Solsvik J. Turbulent channel flow of generalized Newtonian fluids at a low Reynolds number. *J. Fluid Mech.* 2021;908:A43.
18. Anand V, Christov IC. Revisiting steady viscous flow of a generalized Newtonian fluid through a slender elastic tube using shell theory. *J. Appl. Math. Mech.* 2021;101 (2), e201900309.
19. Li S, Dimitrienko YI. Mathematical modeling for the local flow of a generalized Newtonian fluid in 3D porous media. *Appl. Math. Model.* 2022;105:551–565.
20. Reyes R, Ruz O, Bayona-Roa C, Castillo E, Tello A. Reduced order modeling for parametrized generalized Newtonian fluid flows. *J. Comput. Phys.* 2023;484, 112086.
21. Rashid M, Khan MI, Hayat T, Khan MI, Alsaedi A. Entropy generation in flow of ferromagnetic liquid with nonlinear radiation and slip condition. *J. Mol. Liq.* 2019; 276:441–452.
22. Oyelakin IS, Mondal S, Sibanda P. Nonlinear radiation in bioconvective Casson nanofluid flow. *Int. J. Appl. Comput. Math*. 2019;5:1–20.
23. Farooq S, Khan MI, Waqas M, Hayat T, Alsaedi A. Transport of hybrid type nanomaterials in peristaltic activity of viscous fluid considering nonlinear radiation, entropy optimization and slip effects. *Comput. Methods Programs Biomed.* 2020;184, 105086.
24. Al-Khaled K, Khan SU, Khan I. Chemically reactive bioconvection flow of tangent hyperbolic nanoliquid with gyrotactic microorganisms and nonlinear thermal radiation. *Heliyon*. 2020;6(1):e03117.
25. Muhammad T, Waqas H, Khan SA, Ellahi R, Sait SM. Significance of nonlinear thermal radiation in 3D Eyring–Powell nanofluid flow with Arrhenius activation energy. *J. Therm. Anal. Calorim.* 2021;143:929–944.
26. Mabood F, Yusuf TA, Khan WA. Cu-Al_2O_3-H_2O hybrid nanofluid flow with melting heat transfer, irreversibility analysis and nonlinear thermal radiation. *J. Therm. Anal. Calorim.* 2021;143(2):973–984.
27. Kataria HR, Mistry M, Mittal A. Influence of nonlinear radiation on MHD micropolar fluid flow with viscous dissipation. *Heat Transf*. 2022;51(2):1449–1467.
28. Shafiq A, Lone SA, Sindhu TN, Nonlaopon K. Statistical Modelling for the Darcy–Forchheimer Flow of Casson Cobalt Ferrite-Water/Ethylene Glycol Nanofluid under Nonlinear Radiation. *Symmetry*. 2022;14(8):1717.
29. Khan U, Bilal S, Zaib A, Makinde OD, Wakif A. Numerical simulation of a nonlinear coupled differential system describing a convective flow of Casson gold–blood nanofluid through a stretched rotating rigid disk in the presence of Lorentz forces and nonlinear thermal radiation. *Numer. Methods Partial Differ. Equ.* 2022;38(3): 308–328.
30. Gangadhar K, Victoria EM, Lakshmi KB, Chamkha AJ. Nonlinear radiation phenomena for Casson-Maxwell nanoliquid flow with chemical reactions. *Proc. Inst. Mech. Eng.* 2023;237(6):2123–2133.
31. Ahmed F, Reza-E-Rabbi S, Yousuf Ali M, Ali LE, Islam A, Rahman MA, Roy R, Islam MR, Ahmmed SF. Numerical modeling of a MHD non-linear radiative Maxwell nano fluid with activation energy. *Heliyon*. 2024;10(2):e24098.
32. Nandi S, Kumbhakar B. Unsteady MHD free convective flow past a permeable vertical plate with periodic movement and slippage in the presence of Hall current and rotation. *Therm. Sci. Eng. Prog.* 2020;19, 100561.
33. Achogo WH, Okereke IC, Ofomata AI, Amadi OF. Magnetohydrodynamic convective periodic flow through a porous medium in an inclined channel with thermal radiation and chemical reaction. *Int. J. Inn. Sci. and Res. Tech.* 2020;5(1):1129–1139.
34. Al-Mamun A, Arifuzzaman SM, Reza-E-Rabbi S, Alam US, Islam S, Khan MS. Numerical simulation of periodic MHD casson nanofluid flow through porous stretching sheet. *SN Appl. Sci.* 2021;3(2):271.
35. Reza-E-Rabbi S, Ahmmed SF, Islam S, Arifuzzaman SM, Rana BMJ, Yousuf Ali M, Al-Mamun A, Khan MS. Characterization of fluid flow and heat transfer of a periodic magnetohydrodynamics nano non-Newtonian liquid with Arrhenius activation energy and nonlinear radiation. *Heat Transf*. 2022;51(7):6578–6615.
36. Ashraf M, Ilyas A, Ullah Z, Abbas A. Periodic magnetohydrodynamic mixed convection flow along a cone embedded in a porous medium with variable surface temperature. *Ann. Nucl. Energy.* 2022;175, 109218.
37. Patil PM, Goudar B, Patil M, Momoniat E. Bioconvective periodic MHD Eyring-Powell fluid flow around a rotating cone: influence of multiple diffusions and oxytactic microorganisms. *Alex. Eng. J.* 2023;81:636–655.
38. Khedher NB, Ullah Z, Alturki M, Mirza CR, Eldin SM. Effect of Joule heating and MHD on periodical analysis of current density and amplitude of heat transfer of electrically conducting fluid along thermally magnetized cylinder. *Ain Shams Eng.* 2024;15(2), 102374.
39. Yousuf Ali M, Reza-E-Rabbi S, Rasel MMH, Ahmmed SF. Combined impacts of thermoelectric and radiation on hydromagnetic nanofluid flow over a nonlinear stretching sheet. *Partial Differ. Equ. Appl.* 2023;7, 100500.
40. Yousuf Ali M, Reza-E-Rabbi S, Ahmmed SF, Nabi MN, Azad AK, Muyeen SM. Hydromagnetic flow of Casson nano-fluid across a stretched sheet in the presence of thermoelectric and radiation. *Int. J. Thermofluids.* 2024;21, 100484.
41. Yousuf Ali M, Reza-E-Rabbi S, Ahmmed SF. Radiation and hall current impressions on newtonian and bingham fluids flow past a stretching surface. *KU Studies*. 2022: 307–320.
42. Islam MR, Reza-E-Rabbi S, Yousuf Ali M, Rasel MMH, Ahmmed SF. Numerical simulation of mass and heat transport phenomena of hydromagnetic flow of Casson fluid with sinusoidal boundary conditions. *Eng. Rep.* 2023;5(11):e12659.
43. Reza-E-Rabbi S, Yousuf Ali M, Arifuzzaman SM, Khan MS, Ahmmed SF. Numerical modelling of a non-linear radiative non-newtonian nanofluid flow with arrhenius activation energy. *KU Studies*. 2022:291–306.
44. Shah SAA, Ahammad NA, Ali B, Guedri K, Awan AU, Gamaoun F, Tag-ElDin EM. Significance of bio-convection, MHD, thermal radiation and activation energy across Prandtl nanofluid flow: A case of stretching cylinder. *Int. Commun. Heat Mass Transf.* 2022;137, 106299.
45. Shah SAA, Awan AU. Significance of magnetized Darcy-Forchheimer stratified rotating Williamson hybrid nanofluid flow: A case of 3D sheet. *Int. Commun. Heat Mass Transf.* 2022;136, 106214.
46. Shah SAA, Ahammad NA, Din EMTE, Gamaoun F, Awan AU, Ali B. Bio-convection effects on prandtl hybrid nanofluid flow with chemical reaction and motile microorganism over a stretching sheet. *Nanomaterials*. 2022;12(13):2174.
47. Awan AU, Shah SAA, Ali B. Bio-convection effects on Williamson nanofluid flow with exponential heat source and motile microorganism over a stretching sheet. *Chin. J. Phys.* 2022;77:2795–2810.
48. Ali B, Ahammad NA, Awan AU, Oke AS, Tag-ElDin EM, Shah FA, Majeed S. The dynamics of water-based nanofluid subject to the nanoparticle's radius with a significant magnetic field: The case of rotating micropolar fluid. *Sustainability*. 2022; 14(17):10474.
49. Rashed AS, Mahmoud TA, Mabrouk SM. Enhanced Flow and Temperature Profiles in Ternary Hybrid Nanofluid with Gyrotactic Microorganisms: A Study on Magnetic Field, Brownian Motion, and Thermophoresis Phenomena. *J. Appl. Comput. Mech.*. 2024.
50. Yousuf Ali M, Rahman M, Ali MM, Ahmmed SF, Haque S. Data analysis of non-linear radiative electro-periodic MHD flow past a stretching sheet with activation energy impact. *Int. Commun. Heat Mass Transf.* 2024;155, 107572.
51. Mabrouk SM, Inc M, Rashed AS, Akgül A. Similarity analysis of bioconvection of unsteady nonhomogeneous hybrid nanofluids influenced by motile microorganisms. *J. Biol. Phys.* 2024;50(1):119–148.
52. Mabrouk SM, Mahmoud TA, Kabeel AE, Rashed AS. Influence of power-law index and hybrid-nanoparticles concentrations on the behavior of non-Newtonian hybrid nanofluid inside water solar collector. *Mod. Phys. Lett. B.* 2024;38(05), 2350226.
53. Rashed AS, Nasr EH, Mabrouk SM. Influence of Gyrotactic Microorganisms on Bioconvection in Electromagnetohydrodynamic Hybrid Nanofluid through a Permeable Sheet. *Computation*. 2024;12(1):17.
54. Saeed ST, Riaz MB, Baleanu D, Akgul A, Husnine SM. Exact analysis of second grade fluid with generalized boundary conditions. *Intell. Autom. Soft Comput.* 2021;28: 547–559.
55. Awan AU, Abid S, Ullah N, Nadeem S. Magnetohydrodynamic oblique stagnation point flow of second grade fluid over an oscillatory stretching surface. *Results Phys.* 2020;18, 103233.